PREPARATION AND TESTING OF CORROSION- AND SPALLATION-RESISTANT COATINGS

Final Technical Report

Project Reporting Period: October 1, 2011 – June 30, 2016

Prepared for:

AAD Document Control

National Energy Technology Laboratory
U.S. Department of Energy
626 Cochrans Mill Road
PO Box 10940, MS 921-107
Pittsburgh, PA 15236-0940

Cooperative Agreement No. DE-FE0007325

Prepared by:

John P. Hurley

Energy & Environmental Research Center
University of North Dakota
15 North 23rd Street, Stop 9018
Grand Forks, ND 58202-9018

Matthew N. Cavalli

Department of Mechanical Engineering
University of North Dakota
Upson Hall II, Room 266A
243 Centennial Drive, Stop 8359
Grand Forks, ND 58202-8359

2016-EERC-08-11

August 2016

EERC DISCLAIMER

LEGAL NOTICE This research report was prepared by the Energy & Environmental Research Center (EERC), an agency of the University of North Dakota, as an account of work sponsored by the U.S. Department of Energy (DOE) National Energy Technology Laboratory. Because of the research nature of the work performed, neither the EERC nor any of its employees makes any warranty, express or implied, or assumes any legal liability or responsibility for the accuracy, completeness, or usefulness of any information, apparatus, product, or process disclosed or represents that its use would not infringe privately owned rights. Reference herein to any specific commercial product, process, or service by trade name, trademark, manufacturer, or otherwise does not necessarily constitute or imply its endorsement or recommendation by the EERC.

ACKNOWLEDGMENT

This material is based upon work supported by DOE under Award No. DE-FE0007325.

DOE DISCLAIMER

This report was prepared as an account of work sponsored by an agency of the United States Government. Neither the United States Government, nor any agency thereof, nor any of their employees, makes any warranty, express or implied, or assumes any legal liability or responsibility for the accuracy, completeness, or usefulness of any information, apparatus, product, or process disclosed, or represents that its use would not infringe privately owned rights. Reference herein to any specific commercial product, process, or service by trade name, trademark, manufacturer, or otherwise does not necessarily constitute or imply its endorsement, recommendation, or favoring by the United States Government or any agency thereof. The views and opinions of authors expressed herein do not necessarily state or reflect those of the United States Government or any agency thereof.

PREPARATION AND TESTING OF CORROSION- AND SPALLATION-RESISTANT COATINGS

ABSTRACT

The goal of this project was to take a recently developed method of bonding oxide dispersion-strengthened (ODS) FeCrAl plating to nickel superalloys closer to commercial use in syngas-fired turbines. The project was designed to better understand and develop the bonding process and to determine if plating APMT®, a specific highly oxidation-resistant ODS FeCrAl alloy made by Kanthal, onto nickel-based superalloy turbine parts is a viable method for substantially improving the lifetimes and maximum use temperatures of the parts. The superalloys investigated for protection were CM247LC and Rene® 80, both alumina scale-forming alloys. The method for bonding the APMT plate to the superalloys is called evaporative metal bonding, which involves placing a thin foil of zinc between the plate and the superalloy, clamping them together, and heating in an atmosphere-controlled furnace. Upon heating, the zinc melts and dissolves the oxide skins of the alloys at the bond line, allowing the two alloys to diffuse into each other. The zinc then diffuses through the alloys and evaporates from their surfaces, creating a bond between the APMT and the superalloy that is stronger than the APMT itself.

Testing showed that the diffusivity of zinc in both APMT and CM247LC is quite similar at 700°C but 15 times higher in the APMT at 1214°C. Coefficients of thermal expansion were determined for each of the alloys as a function of temperature. This information was entered into a finite-element model using ANSYS, which was used to design a clamping jig for pressing the APMT to the superalloys at the bonding temperature. Scanning electron microscopy analyses of representative joints showed that no zinc remained in the alloys after bonding Unfortunately, the analyses also showed some small pieces of broken aluminum oxide scale near the bond lines, indicating that its scale was not sufficiently removed during prebonding cleaning. Samples from each of the bonded blocks were sent to Siemens for its standard oxidation, spallation, and corrosion testing, which was scheduled for completion in the spring of 2016. However, because of commercial demands, the tests were not completed by the time of this report except some initial spallation tests at 1150°C. In those tests, several of the APMT plates separated from the CM247LC, likely because of the remaining aluminum oxide scale on the surface of the CM247LC. This implies that surface preparation may need to include machining to remove the oxide scale before bonding rather than just sandblasting. In previous tensile testing at 950°C, the breaks in the tensile samples always occurred in the APMT and not at the joints.

Gasifier sampling was completed to determine what types of trace contaminants may occur in cleaned and combusted syngas and that could lead to corrosion or deposition in turbines firing coal syngas. The sampling was done from a pressurized fluidized-bed gasifier and a pressurized entrained-flow gasifier. The particles captured on a filter from syngas were typically 0.2 to 0.5 µm in diameter, whereas those captured from the combusted syngas were slightly larger and more spherical. X-ray photoelectron spectroscopy done at Oak Ridge National Laboratory showed that the particles do not contain any metals and have an atomic composition almost identical to that of the polycarbonate filter. This indicates that the particles are primarily soot-based and not formed from volatilization of metals in the gasifiers.

TABLE OF CONTENTS

LIST OF FIGURES

Continued…

LIST OF FIGURES (continued)

Continued…

LIST OF FIGURES (continued)

LIST OF TABLES

NOMENCLATURE

AES	Auger electron spectroscopy
APMT®	oxide dispersion-strengthened FeCrAl alloy made by Kanthal
ASME	American Society of Mechanical Engineers
BEI	backscatter electron imaging
CBS	circular backscatter
CM247LC	alumina scale-forming nickel-based superalloy
CVAAS	cold-vapor atomic absorption spectrometry
EDM	electrodischarge machining
EDS	energy-dispersive spectroscopy
EERC	Energy & Environmental Research Center
EFG	entrained-flow gasifier
EMB	evaporative metal bonding
EPA	U.S. Environmental Protection Agency
FBG	fluidized-bed gasifier
HGFV	hot-gas filter vessel
IC	ion chromatography
ICP	inductively coupled plasma
LLQ	lower limit of quantification
M	method
MS	mass spectrometry
ODS	oxide dispersion strengthened
ORNL	Oak Ridge National Laboratory
Rene® 80	alumina scale-forming nickel-based superalloy
SEI	secondary electron imaging
SEM	scanning electron microscopy
TOX	thermal oxidizer
TZM	titanium–zirconium-strengthened molybdenum
UND	University of North Dakota
UTSR	University Turbine Systems Research
XPS	x-ray photoelectron spectroscopy

PREPARATION AND TESTING OF CORROSION-AND SPALLATION-RESISTANT COATINGS

EXECUTIVE SUMMARY

The goal of this project was to take a recently developed method of bonding oxide dispersion-strengthened (ODS) FeCrAl plating to nickel superalloys closer to commercial use in syngas-fired turbines. The project was designed to better understand and develop the bonding process and to determine if plating APMT®, a specific highly oxidation-resistant ODS FeCrAl alloy made by Kanthal, onto nickel-based superalloy turbine parts is a viable method for substantially improving the lifetimes and maximum use temperatures of the parts. The superalloys investigated for protection were CM247LC and Rene® 80, both alumina scale-forming alloys. The method for bonding the APMT plate to the superalloys is called evaporative metal bonding (EMB), which involves placing a thin foil of zinc between the plate and the superalloy, clamping them together, and heating in an atmosphere-controlled furnace. Upon heating, the zinc melts and dissolves the oxide skins of the alloys at the bond line, allowing the two alloys to diffuse into each other. The zinc then diffuses through the alloys and evaporates from their surfaces, creating a bond between the APMT and the superalloy that is stronger than the APMT itself.

The work was divided into six tasks. Task 1 was the project management and planning task. Task 2 was to measure and model the diffusion rates of zinc through the three alloys as functions of temperature. Task 3 involved the development of a model to allow us to calculate the stress distribution created by clamps holding together the metal pieces that are being bonded by the EMB process so that an appropriate clamping system could be designed depending on the shapes of the parts being bonded together. Task 4 was to determine what minor ash-forming constituents were present in combusted coal syngas that could contribute to corrosion of the bonded alloys, and then use that information to design corrosion tests of the bonded alloys unless only soot was detected, in which case Siemens would perform its standard corrosion tests. Task 5 was to use the diffusion and clamping models developed in Tasks 2 and 3 to design a firing schedule and clamping system to bond APMT plate to superalloy turbine or other parts supplied by Siemens and then bond the APMT plate to the superalloy parts. Task 6 was to perform spallation, oxidation, and corrosion testing of the bonded parts. Tasks 1–5 were performed by the University of North Dakota (UND), while most of the Task 6 work was to be performed by Siemens without funding from this University Turbine Systems Research (UTSR) Program, nor was that work used as a portion of the cost share for the project.

We have found that we were unable to create joints when temperatures much lower than the original (pre-UTSR Program) temperature of 1214°C were used. Therefore, we limited our diffusion rate measurements to the two hold temperatures used in the procedure: 700° and 1214°C. The diffusivity of zinc in both APMT and CM247LC is quite similar at 700°C. At 1214°C, the situation is very different. The calculated diffusivity of zinc in APMT is approximately 15 times higher than in CM247LC or Rene 80 (~120 vs. ~8 μm^2/min) at that temperature.

In addition to the diffusion work, the coefficients of thermal expansion were determined for each of the alloys as a function of temperature. This information has been entered into a finite-

element model using ANSYS so that appropriate force-applying structures can be designed for use in joining structures composed of APMT and the nickel alloys. The finite-element model was completed and used to design clamping jigs to hold 1-mm-thick APMT plate to the larger blocks of superalloys during the bonding process. The clamping system was machined from titanium–zirconium-strengthened molybdenum because of its strength at temperature and lower coefficient of thermal expansion than any of the alloys being bonded. Scanning electron microscopy (SEM) analyses of representative joints showed that no zinc remained in the alloys after bonding. Also, phases rich in hafnium and tantalum had precipitated near the bond line in the APMT. Iron from the APMT had diffused into the superalloys during bonding, more extensively in the CM247LC than in the Rene 80. Nickel from the superalloys had diffused into the APMT, again more extensively in the joint with the CM247LC than with the Rene 80. Unfortunately, the analyses also showed some small pieces of broken aluminum oxide scale near the bond lines. One-inch-diameter buttons were machined from each of the bonded blocks and sent to Siemens for standard oxidation, spallation, and corrosion testing, which was scheduled for completion in the spring of 2016. However, because of commercial demands on those at Siemens who were to do the testing, the tests were not completed by the time of this report except some initial spallation tests at 1150°C. In those tests, several of the APMT plates separated from the CM247LC, likely because of the aluminum oxide that was present on the surface of the CM247LC. This implies that surface preparation may need to include machining to remove the oxide scale before bonding rather than just sandblasting. In previous tensile strength testing of APMT–CM247LC joints that were surface-machined before bonding and tested at 950°C, the breaks in the tensile samples always occurred in the APMT and not at the joints.

Gasifier sampling was completed to determine what types of trace contaminants may occur in cleaned and combusted syngas and that could lead to corrosion or deposition in turbines firing coal syngas. The sampling was done from two EERC pilot-scale gasifiers that were being operated under funding outside of the UTSR Program. One is a pressurized fluidized-bed gasifier and the other a pressurized entrained-flow gasifier. SEM analyses showed that the particles captured on the filter from the syngas were typically 0.2 to 0.5 µm in diameter, whereas those captured from the combusted syngas were slightly larger and more spherical. X-ray photoelectron spectroscopy was performed on the samples at Oak Ridge National Laboratory. The data showed that the particles do not contain any metals and, in fact, have an atomic composition almost identical to that of the polycarbonate filter. We currently believe that this indicates that the particles are primarily soot-based and not formed from volatilization of metals in the gasifiers. The data indicate that the soot-based particles are not well burned in a thermal oxidizer, although they are significantly oxidized, nitrided, and sulfidized in the combustor at the particle surfaces.

PREPARATION AND TESTING OF CORROSION- AND SPALLATION-RESISTANT COATINGS

INTRODUCTION

The goal of this University of North Dakota (UND) (Energy & Environmental Research Center [EERC] and Department of Mechanical Engineering) project was to take a recently developed method of bonding oxide dispersion-strengthened (ODS) FeCrAl plating to nickel superalloys closer to commercial use in syngas-fired turbines. The project was designed to better understand and develop the bonding process and to determine if plating APMT®, a specific highly oxidation-resistant ODS FeCrAl alloy made by Kanthal, onto nickel-based superalloy turbine parts is a viable method for substantially improving the lifetimes and maximum use temperatures of the parts. The superalloys investigated for protection were CM247LC and Rene® 80, both alumina scale-forming alloys. The compositions of the alloys are given in Table 1. The method for bonding the APMT plate to the superalloys is called evaporative metal bonding (EMB), which involves placing a thin foil of zinc between the plate and the superalloy, clamping them together, and heating in an atmosphere-controlled furnace. Upon heating, the zinc melts and dissolves the oxide skins of the alloys at the bond line, allowing the two alloys to diffuse into each other. The zinc then diffuses through the alloys and evaporates from their surfaces, creating a bond between the APMT and the superalloy that is stronger than the APMT itself.

Table 1. Compositions of Base Metals, wt%

Alloy	Fe	Ni	Cr	Al	Ti	Co	Mo	Ta	W
AMPT	68.9		22	5			3		
CM247LC	–	61.4	8.1	5.6	0.7	9.5	0.5	3.2	9.5
Rene 80	0.10	61.9	13.4	2.1		9.4	4.1		
Alloy	**Nb**	**Hf**	**Mn**	**Si**	**C**	**W**	**Ti**	**B**	**Zr**
AMPT			0.4	0.7					
CM247LC	0.1	1.4	–	–					
Rene 80	0.03				0.16	3.92	4.77	0.02	0.04

The work was divided into six tasks. Task 1 was the project management and planning task. Task 2 was to measure and model the diffusion rates of zinc through the three alloys as functions of temperature. Task 3 involved the development of a model to allow us to calculate the stress distribution created by clamps holding together the metal pieces that are being bonded by the EMB process so that an appropriate clamping system could be designed depending on the shapes of the parts being bonded together. Task 4 was to determine what minor ash-forming constituents were present in combusted coal syngas that could contribute to corrosion of the bonded alloys, and then use that information to design corrosion tests of the bonded alloys unless only soot was detected, in which case Siemens would perform its standard corrosion tests. Task 5 was to use the diffusion and clamping models developed in Tasks 2 and 3 to design a firing schedule and clamping system to bond APMT plate to superalloy turbine or other parts supplied by Siemens and then bond the APMT plate to the superalloy parts. Task 6 was to perform spallation, oxidation, and corrosion testing of the bonded parts. Tasks 1–5 were performed by UND, while most of the Task 6 work was to be performed by Siemens; however, because of other commercial obligations, Siemens was not able to perform this work by the project end date of June 30, 2016.

EXPERIMENTAL METHODS

Laboratory Testing and Modeling

Under Tasks 2 and 3, we measured properties of the alloys and developed computer models of their high-temperature properties in order to develop the best methods for joining the APMT plate to CM247LC and Rene 80 parts. In order to determine the best heating schedules to use for joining APMT plates to superalloy parts, we measured the diffusion rates of zinc through the alloys as a function of temperature. Two temperatures were the focus of the diffusion work, 700° and 1214°C, because those are hold temperatures in the EMB process. In order to develop the best clamp designs to use for holding the plating to the parts, we also measured coefficients of thermal expansion of the materials as functions of temperature. Once the bonding clamp design was modeled, a clamping system was machined out of titanium–zirconium-strengthened molybdenum (TZM) because of its strength and low coefficient of thermal expansion.

Figure 1 shows a) the assembled bonding jig and sample and b) the separate bonding components that were used for the Task 2 diffusion testing. This clamping jig is a design used before the University Turbine Systems Research (UTSR) Program. The jig assembly (body plus bolt) is fabricated from TZM because of its low thermal expansion. The two rods that were bonded were composed of the same metal so that the diffusion rate of zinc into that metal could be determined.

Spherical steel (E52100) end caps were used to help with alignment of the bonding sample by allowing it to articulate to make sure that the clamping force is evenly distributed across the joint between the two alloy cylinders.

The bonding was achieved using the following process:

1) Bonding samples cut from larger rods using electrodischarge machining (EDM)
2) Bonding surfaces polished to 180 grit
3) Entire surface of bonding samples sandblasted
4) Bonding surfaces polished to 220 grit
5) Bonding samples, end caps, bolt, and jig ultrasonically cleaned in acetone
6) Bonding samples, end caps, bolt, and jig cleaned in isopropanol
7) Pieces clamped together
8) Clamped assembly heated under a controlled atmosphere to effect the EMB joint

Steps 2 and 4 were found to be necessary because the pressure distribution across the bonding surface is not uniform when the bonding assembly used bonding samples that had just undergone EDM. After bonding, the pieces were cut lengthwise and polished and then analyzed in a scanning electron microscope to determine the extent of zinc diffusion into the alloys.

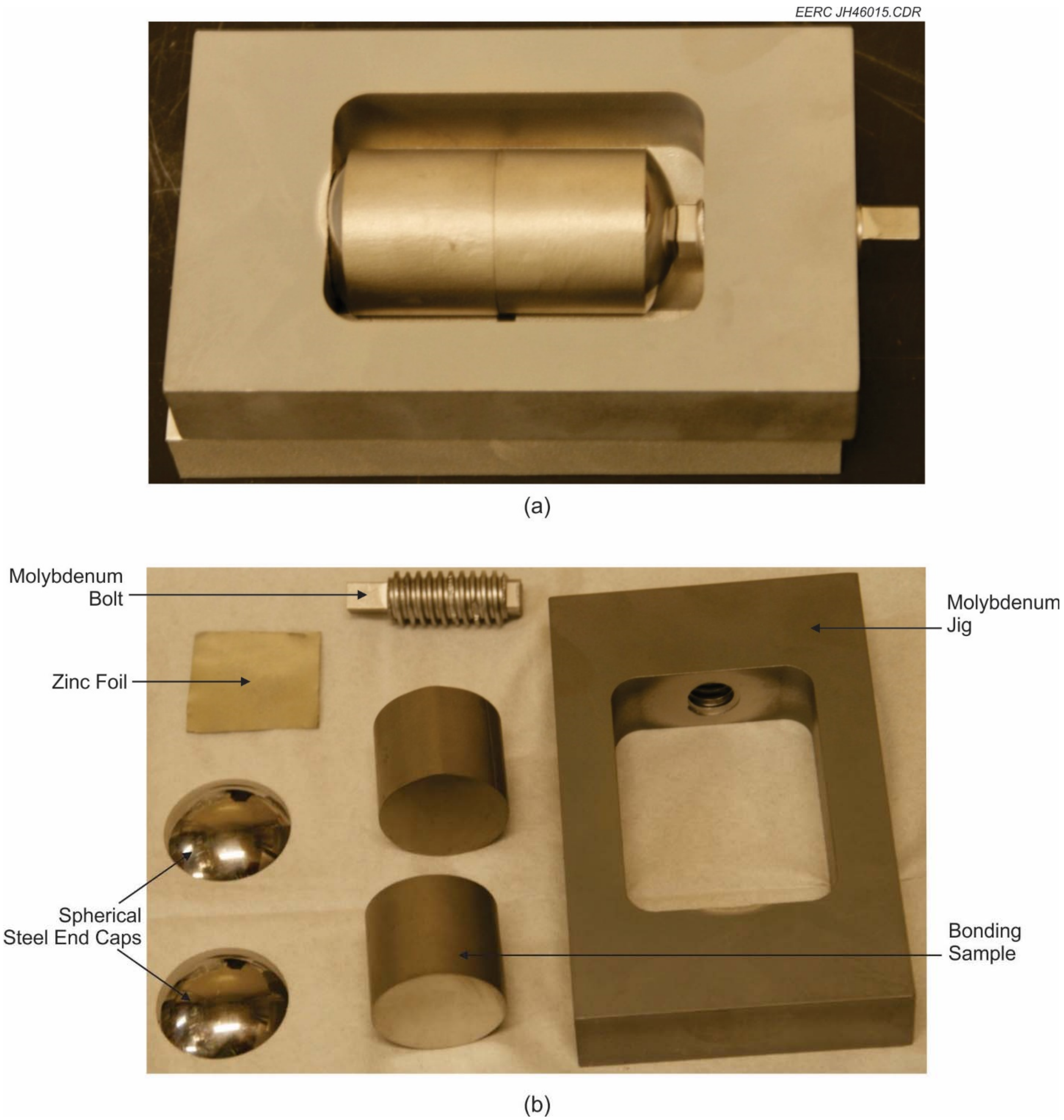

Figure 1. a) Assembled bonding jig and sample and b) separate bonding components used in the diffusion testing.

Under Task 3 the coefficients of thermal expansion of the three alloys (APMT, CM247LC, and Rene 80) were determined as functions of temperature using a thermomechanical analyzer. These data were entered into an ANSYS finite-element model for calculating expected pressures during EMB processing in order to develop a design for the clamping jigs to be used during the actual bonding process. Under Task 5, the parts to be joined were then clamped together and heated in a controlled atmosphere to cause the 1-mm-thick APMT plate to be bonded to the surfaces of the superalloy slabs provided by Siemens. A description of the overall bonding jig that was designed is given in the results and discussion section of this report. Cylinders or buttons of the bonded materials were then machined and sent to Siemens for its standard oxidation, spallation, and corrosion testing so that the results for the APMT-plated parts could be compared to data from tests of nonplated parts.

Gasifier Sampling

In addition to the laboratory testing, under Task 4 we sampled combusted syngas created in two pilot-scale coal gasifiers to determine what types of trace contaminants may occur in cleaned syngas that could lead to corrosion issues in turbines firing syngas. The EERC has several pilot-scale gasifiers that are continually used in a variety of test configurations. Funding for the actual operation of the gasifiers comes from projects other than the UTSR project. The trace contaminants were collected using standard U.S. Environmental Protection Agency (EPA) sampling techniques before and after the syngases were burned in a refractory-lined thermal oxidizer (TOX). Initially, the sampling trains used were for EPA Method (M) 29 sampling for particulate- and vapor-phase metals and M26A for halogens. Later, it was found that the halogens or metals detected were near or below the minimum detection levels for the analytical instruments so sampling was later done with just a surface filter.

One gasifier is a pressurized entrained-flow gasifier (EFG), and the other is a pressurized fluidized-bed gasifier (FBG). Figure 2 shows a cross-sectional view of the EFG. The EFG is a dry-feed, downfired system. The reactor tube is vertically housed in a pressure vessel approximately 24 in. in diameter and 7 ft in length. The EFG fires nominally 8 lb/hr of coal and produces up to 20 scfm of fuel gas. The maximum allowable working pressure is 300 psig. The reactor has the capability to run in oxygen- or air-blown mode. The supplemental electrical heating system is capable of reaching a nominal temperature of 1500°C (2732°F) and is separated into four independent zones so that a consistent temperature can be maintained throughout the length of the furnace. The radially spaced heating elements provide the initial heat for the centrally located alumina reactor tube, and refractory walls outside the heating elements provide insulation. Type S thermocouples are used to monitor and control the temperatures of the heating zones and reactor tube. All of the gasification reactions occur inside the reactor tube, and slag is able to flow on the tube walls. Pressure inside the alumina reactor tube is balanced with a slightly positive nitrogen pressure outside of the alumina reactor tube.

Pulverized coal is fed into the top of the furnace via a twin-screw feeder and scale contained in a pressurized vessel. A lock hopper is in place that allows the system to be refilled while running, thereby facilitating continuous-mode operation. Feed rates are calculated in real time. Nitrogen is used to convey the solid pulverized coal into the combustion zone.

Product gas exits at the bottom of the furnace tube and enters a reducing section that houses a quench system capable of injecting water, syngas, or nitrogen as the quench fluid. The product gas then enters a cross, making a 90° turn, and then exits the main unit on its way to the back-end

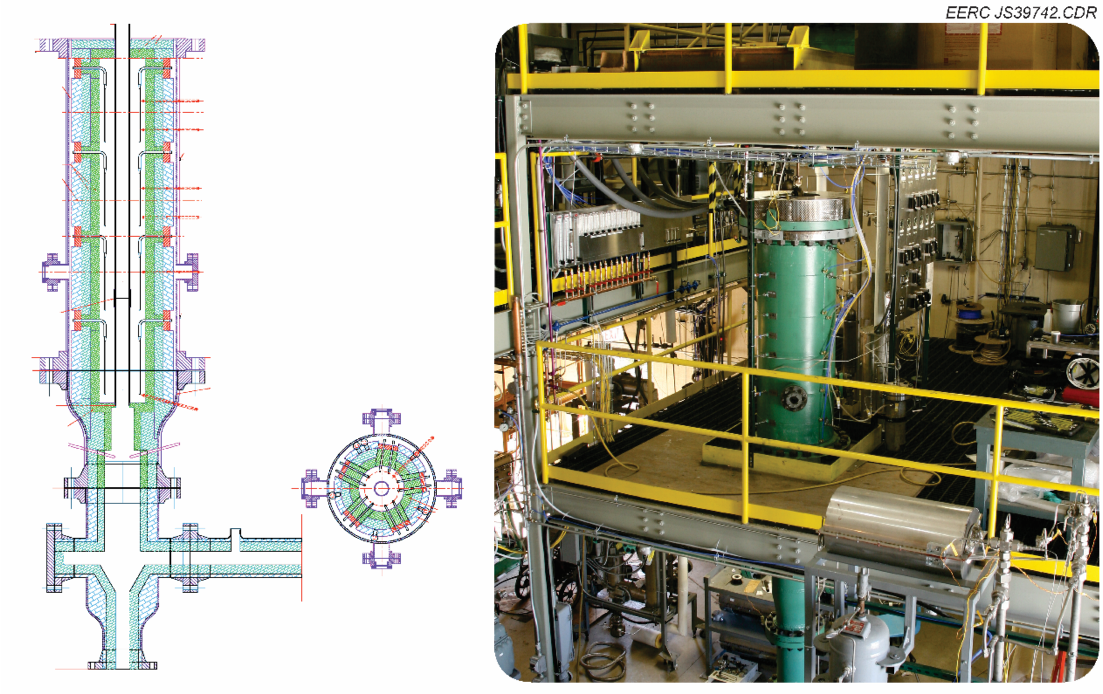

Figure 2. EFG.

control devices. Slag, ash, and char drop through the cross and are collected in a refractory-lined slag trap. Fine particulate is able to flow with the gas through the 90° turn and is collected in a downstream filter.

The overall system layout for the test run is shown in Figure 3. Slag is collected below the gasifier in a refractory-lined slag trap. Fly ash is captured in the hot-gas filter vessel (HGFV) that uses an iron aluminide candle filter, providing near-absolute filtration. The gas then passes through water–gas shift reactors that can shift sour gas (containing H_2S) to increase its H_2 concentration. A portion then goes through sulfur adsorbers and then to hydrogen separation membranes that were tested during most runs. The portion not going to the separation membranes is quenched to remove moisture and any tars formed in the system. All gas streams, including the membrane raffinate and permeate streams, are then recombined before combusting them in the TOX. Initially, samples were collected only at the exit of the TOX, but in later tests, samples were collected both before and after the TOX.

The pressurized FBG was designed according to American Society of Mechanical Engineers (ASME) B31.3 Process Piping Code specifications. After a review of available alloys, Haynes 556® was selected as the material most suitable for fabrication of this high-temperature, high-pressure system. The reactor was designed with the capability to operate at 6.9 MPa (1000 psig) at an operational temperature of 843°C (1550°F), 4.5 MPa (650 psig) at an operational temperature of 917°C (1650°F), and 2.0 MPa (300 psig) at an operational temperature of 1800°F. This system is externally electrically heated. Haynes 556 alloy was used for construction of the reactor, all the reactor nozzles, and the cyclone. A design drawing of the reactor is shown in Figure 4, and a photograph of the gasifier is shown in Figure 5.

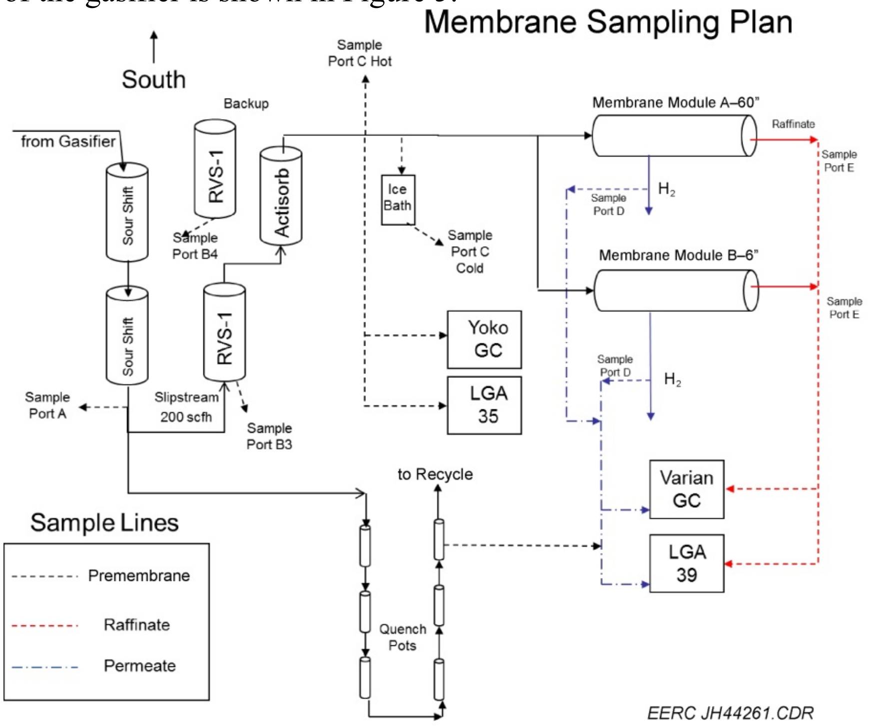

Figure 3. EFG equipment used to produce the syngas sampled for most tests during this program.

The FBG is capable of feeding up to 9.0 kg/hr (20 lb/hr) of pulverized coal or biomass at pressures up to 70 bar absolute (1000 psig). The externally heated bed is initially charged from an independent hopper with silica sand, but through time the bed converts to coal ash. Independent mass flow controllers meter the flow of nitrogen, oxygen, steam, and recycled syngas into the bottom of the fluid bed. Various safety interlocks prevent the inadvertent flow of pure oxygen into the bed or reverse flow into the coal feeder. Recycled syngas is injected several inches above the bottom distributor plate, which prevents direct combustion of syngas with oxygen entering at the bottom of the bed.

During operation of the system, fly ash was captured in a HGFV that uses an iron aluminide candle filter, providing near-absolute filtration. The gas then passed through water–gas shift reactors that can shift sour gas (containing H_2S) to increase its H_2 concentration. The gas then passed through water quench pots to remove tars and a portion of the H_2S. A portion of this gas was then sent to a piece of technology that was the reason for the tests, and the rest was combusted in the TOX from which the syngas samples were collected. Approximately 85% of the 2500 ppm of H_2S in the gas was removed with a zinc-based fixed-bed sorbent system before the TOX. The gas that was passed through the special equipment being tested during this run was flared separately.

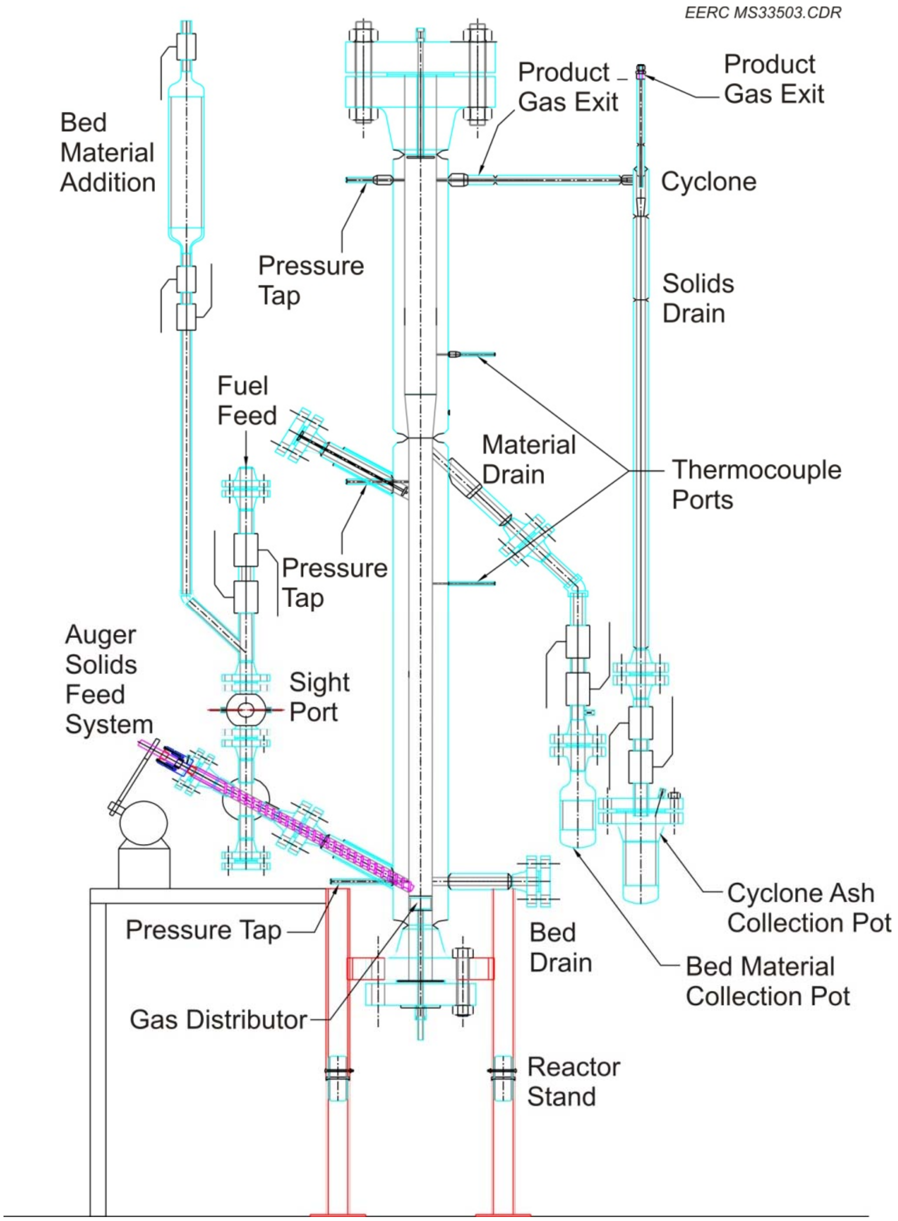

Figure 4. Design drawing of the pressurized fluidized-bed gasification reactor.

The FBG operates at lower temperatures than the EFG. As a result, more CH_4 is produced by the FBG, and it was also expected that more fine, metal-rich particulates would be formed in the EFG that could possibly pass through the system filters and reach a turbine firing syngas from an EFG. Hydrogen concentration in the dry gas resided in the 40% range during the tests. CO was in the 2.5% range, while CO_2 was in the low-50% range in the dry gas. The high CO_2 concentration indicated that the sour gas shift catalysts were operating correctly. CH_4 typically runs at about 3%. Hydrocarbons and trace organics may also be produced by the FBG. These are largely dependent on fuel type and operational parameters. The N_2 purge requirements of the FBG are substantially lower than for the EFG, resulting in much lower N_2 dilution of approximately 3% of the dry gas.

Figure 5. Photograph of the high-pressure FBG.

The TOX contains a burner at the top of a refractory-lined chamber that admits the syngas and air separately and also includes a premixed natural gas and air supplemental gas stream. An accurate flame temperature is not available for the TOX because thermocouples burn out too quickly in the flame. The sampling occurs at the bottom of the downfired oxidizer. The gas being sampled is at approximately 750°C. It is quenched as it is pulled through the glass sampling tube to approximately 100°C before reaching the filter. The sampling train initially consisted of a one-piece glass nozzle–probe liner, a large particulate cyclone, and the polycarbonate surface filter with 0.2-µm holes (Whatman™ Nuclepore™ type with a melting temperature of 250°C), followed by a series of impingers (five for M26A and six for M29), shown in Figure 6. Impingers were of a standard Greenburg–Smith design type and connected in series with leak-free ground brass fittings. However, it was found that the concentrations of elements collected in the impingers were consistently very close to or below the minimum detection limits of the analytical instruments used, and so in later tests, only the filter was used to collect microconstituents in the syngas and its combustion products.

M26A is applicable for the determination of hydrogen halide (HCl, HBr, and HF) and halogen (Cl_2 and Br_2) emissions from stationary sources. The impinger solutions are analyzed by ion chromatography (IC), which detects and quantifies the amount of F^-, Cl^-, and Br^- ions in these solutions. The concentration of a target hydrogen halide or halogen emission in solution is suggested to be greater than the corresponding lower limit of quantification (LLQ) to be detected by the IC system. The minimum detection limit for bromide, chloride, and fluoride is 1 mg/L using the EERC equipment for M26A.

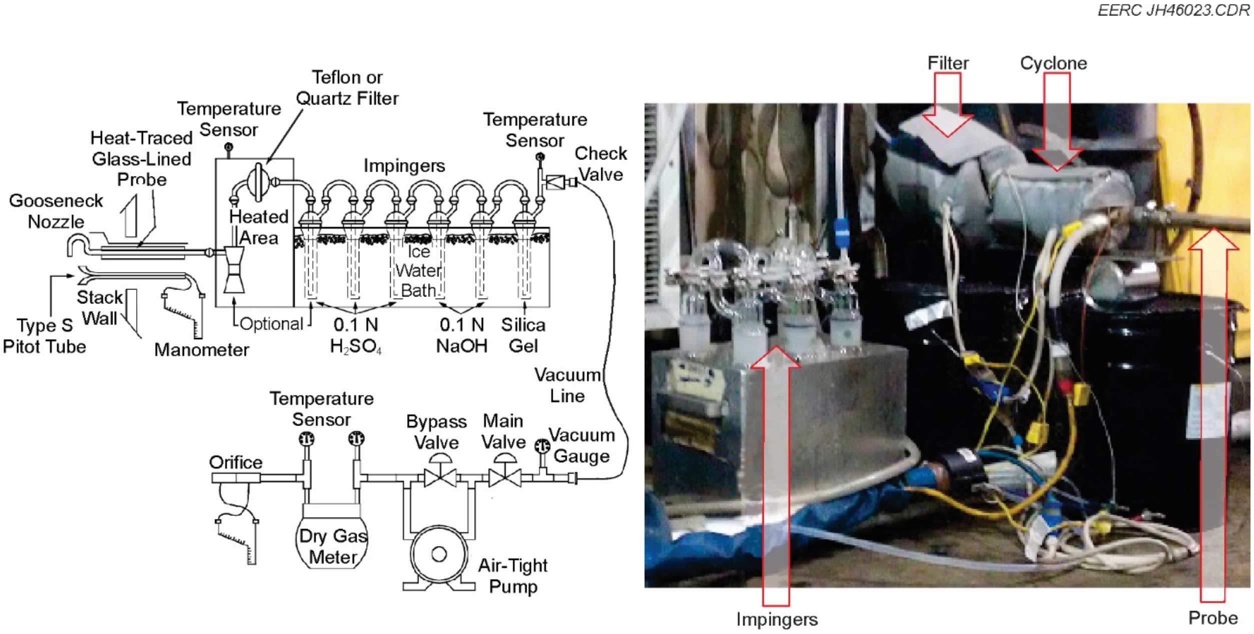

Figure 6. M29 and 26A sampling train.

M29 is applicable to the determination of EPA-designated hazardous metal emissions such as lead (Pb), nickel (Ni), manganese (Mn), mercury (Hg), selenium (Se), cadmium (Cd), chromium (Cr), silver (Ag), thallium (Tl), arsenic (As), antimony (Sb), barium (Ba), beryllium (Be), cobalt (Co), phosphorus (P), zinc (Zn), and copper (Cu) from stationary sources. Initially, we only analyzed for those elements, but in later tests, we also analyzed for major elements; however, their concentrations were also near or below the minimum detection limits of the analyzers used for the solutions so later tests were done only with the surface filter. The filters were analyzed using scanning electron microscopy (SEM), impinger solutions were analyzed using different spectroscopic techniques such as cold-vapor atomic absorption spectrometry (CVAAS) for Hg, and inductively coupled plasma–mass spectrometry (ICP–MS) for the remaining trace metals. The minimum detection limits for the trace metals analyzed in this work are presented in Table 2.

Table 2. Limit of Detection of Trace Metals Analyzed

Trace Metal:	**As**	**Be**	**Cd**	**Co**	**Cr**	**Mn**	**Ni**	**Pb**	**Sb**	**Se**
LLQ, µg/L	0.5	0.1	0.1	0.5	0.1	0.1	0.2	0.1	0.1	1.0

RESULTS AND DISCUSSION

Laboratory Testing

Zinc Diffusion Rates

After bonding rods of each of the alloys to themselves using the EMB technique, each joint was sectioned parallel to the sample axis (perpendicular to the bond line) and analyzed via SEM and energy-dispersive spectroscopy (EDS). EDS data were then used to estimate the diffusivity of zinc in each alloy at each temperature based on Equation 1 [1]:

$$C(x,t) = \frac{\beta}{2\sqrt{\pi D^* t}} exp\left(\frac{-x^2}{4D^* t}\right) \qquad \text{[Eq. 1]}$$

where β is the initial concentration of diffusing species, D* is the diffusivity, t is time, and x is distance from the midline. Originally, it was planned that we would determine the diffusion rates at several different temperatures in order to determine bonding times at various temperatures. However, we have found that we were not able to create joints when temperatures much lower than the original temperature of 1214°C are used. Therefore, we limited our diffusion rate measurements to the two hold temperatures used in the procedure: 700° and 1214°C.

Table 3 shows diffusivity calculations for the APMT and CM247LC at 700°C. The units are given as volume/distance/time. No usable results were able to be obtained for the Rene 80 samples at this temperature. Table 4 shows the calculated diffusivities for APMT, CM247LC, and Rene 80 at 1214°C. In both tables, “Center” indicates composition data taken from the midline of the sectioned joints. “Edge” indicates composition data taken from the outer limit of the bonded region. This is illustrated in Figure 7. The apparent higher diffusion rate measured at the edge is greater than that at the center because the method is based on changes in composition with distance, and near the edges, zinc evaporates from the surface, creating a more rapid apparent diffusion rate.

Table 3. Calculated Diffusivities of Zinc in APMT and CM247LC at 700°C Based on EDS Data

Material	Temp., °C	Time, min	Center D, μm^2/min	Edge D, μm^2/min
APMT	700	30	3.29	4.10
CM247LC	700	30	1.23	1.81

Table 4. Calculated Diffusivities of Zinc in APMT, CM247LC, and Rene 80 at 1214°C Based on EDS Data

Material	Temp., °C	Time, min	Center D, μm^2/min	Edge D, μm^2/min
APMT	1214	60	103.57	142.58
	1214	300	130.82	N/A[1]
CM247LC	1214	60	5.33	15.66
	1214	180	8.55	7.13
	1214	300	3.71	3.75
	1214	600	5.87	N/A
	1214	1200	1.17	N/A
Rene 80	1214	60	15.64	9.37
	1214	180	9.66	8.79
	1214	300	8.31	6.96
	1214	600	3.00	N/A
	1214	1200	6.21	N/A

[1] Not analyzed.

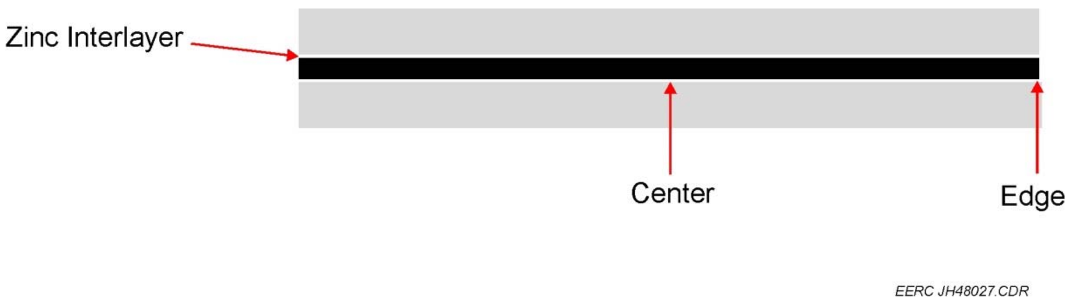

Figure 7. Schematic showing location of center and edge data.

Table 5 shows the center line composition of each of the joints from Tables 3 and 4 (data taken at the center position of each joint).

Table 5. Center Line Concentration of Each Joint, wt% zinc

Material	Temp., °C	Time, min	Center Concentration, wt%
APMT	700	30	16.2
	1214	60	2.6
	1214	300	1.9
CM247LC	700	30	16.7
	1214	60	6.9
	1214	180	4.1
	1214	300	3.5
	1214	600	3.7
	1214	1200	2.1
Rene 80	1214	60	8.1
	1214	180	6.8
	1214	300	4.8
	1214	600	2.7
	1214	1200	1.4

Several observations can be made about the data in Tables 3–5. First, the diffusivity of zinc in both APMT and CM247LC is quite similar at 700°C. Diffusivity in the APMT appears to be slightly higher (~4 vs. ~2 μm^2/min), but the midline composition after 30 minutes at this temperature is quite similar. At 1214°C, the situation is very different. Because only about 15 wt% zinc remained at the midline after the low-temperature hold, the absolute difference in zinc concentrations between the APMT, CM247LC, and Rene 80 at 1214°C is relatively small. However, the calculated diffusivity of zinc in APMT is approximately 15 times higher than in CM247LC or Rene 80 (~120 vs. ~8 μm^2/min) at 1214°C. Equation 2 is the standard expression for diffusivity in terms of the diffusion coefficient, D_o, and the activation energy for diffusion, Q, where R is the ideal gas constant and T is the absolute temperature:

$$D^* = D_o exp\left(\frac{-Q}{RT}\right) \quad \text{[Eq. 2]}$$

If D_o and Q are assumed to be independent of temperature and composition for each material system and the approximate ratio of the diffusivities calculated above is substituted into Equation 2 for APMT and CM247LC, the difference in activation energies for diffusion of zinc through the two alloys can be estimated. This calculation yields:

$$Q_{CM247} - Q_{APMT} \cong -54\frac{kJ}{kmol} \quad \text{[Eq. 3]}$$

For reference, this value is similar in magnitude and sign to the difference in activation energies for the diffusion of copper in pure nickel (258 kJ/kmol) and pure iron (295 kJ/kmol) [2].

Modeling Bonding Pressures

Expansion coefficients of each of the metals which were either bonded together or used to make the clamps that held the alloys during bonding were determined in laboratory tests using a thermomechanical analyzer. Table 6 shows the linear coefficient of thermal expansion as a function of temperature for each of the materials used in this study (parent materials and clamping jig materials). Each value is the average of four measurements. The units are microstrain/°C, sometimes given as $\times 10^{-6}$/°C. These data were entered into a finite-element model of the sample and jig to determine the stress distribution within the joint during bonding.

Table 6. Linear Coefficient of Thermal Expansion (α) as a Function of Temperature for Each Material Involved with the Bonding Process

Temperature, °C	APMT, 10^{-6}/°C	CM247LC, 10^{-6}/°C	Rene 80, 10^{-6}/°C	Mo, 10^{-6}/°C	Steel, 10^{-6}/°C
100	13.0	13.2	14.0	7.5	16.0
200	14.4	14.3	14.7	8.5	18.1
300	16.5	15.4	15.5	10.0	20.6
400	17.9	16.2	16.2	10.9	21.9
500	18.6	16.9	16.7	11.5	22.6
600	18.8	17.3	17.0	11.7	23.0
700	19.3	17.7	17.5	11.9	23.2
800	19.6	18.0	17.9	12.1	21.9
900	20.0	18.3	18.4	12.1	22.2
1000	20.5	18.3	19.1	13.3	22.5
1100	21.0	17.5	20.3	14.7	22.7
1200	21.2	16.9	21.3	15.2	23.0

Final finite-element modeling using ANSYS was done to determine the clamping jig geometry for fabrication of the specimens for oxidation/spallation/corrosion testing. All parts of the jig are made from TZM because it has a lower coefficient of thermal expansion than the parts being bonded, so those parts are put in compression upon heating of the assembly. Figure 8 shows several views of the assembly that was used to fabricate the specimens. Figure 8a is an isometric view, while Figures 8b and c are side and end views, respectively. Figure 8c also shows each piece of the assembly labeled with the material type.

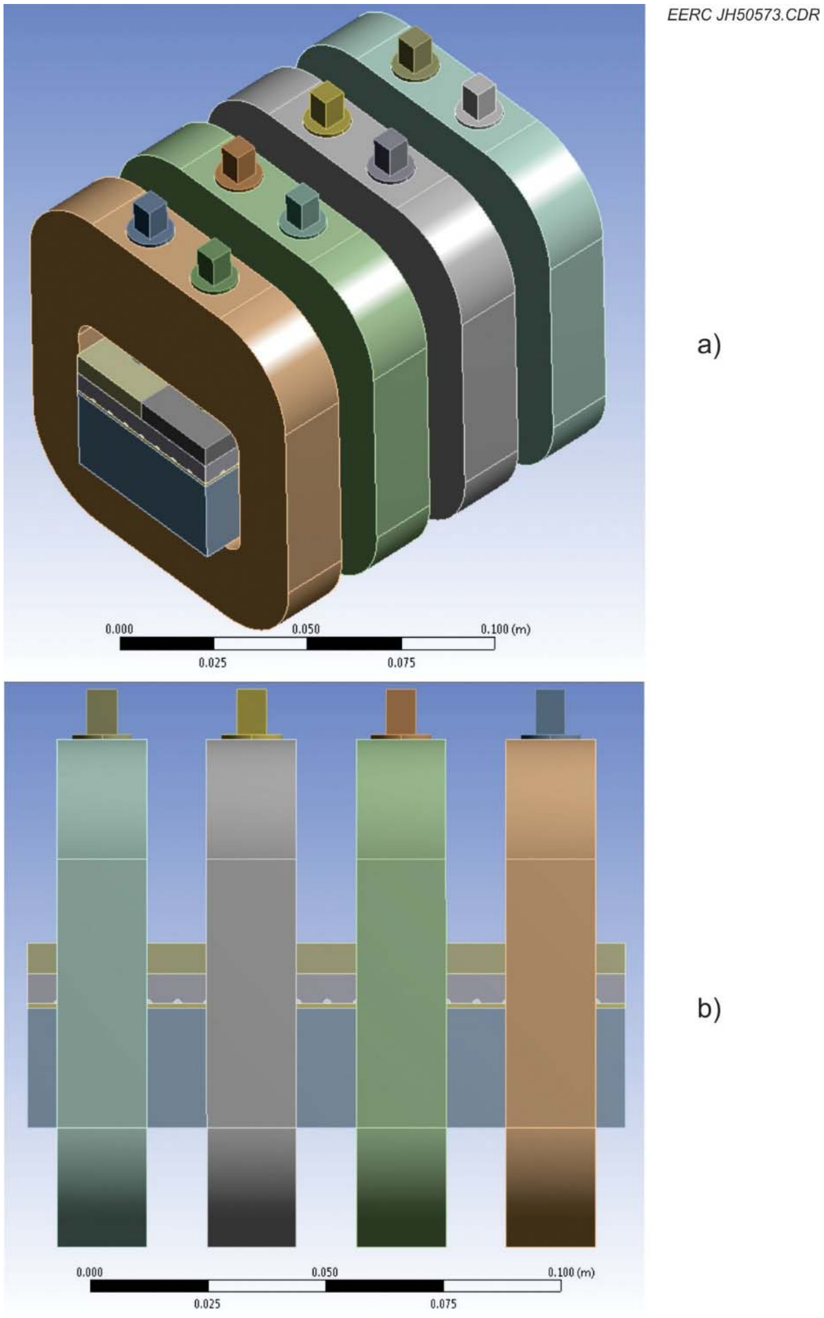

Figure 8. Jig assembly used for fabrication of the test samples (continued. . .).

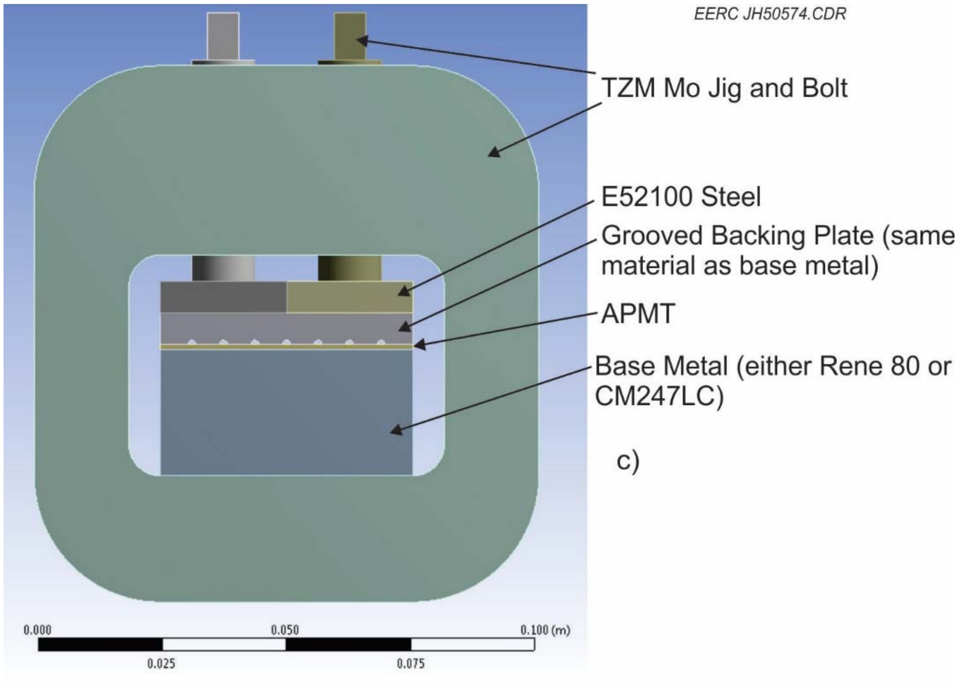

Figure 8 (continued). Jig assembly used for fabrication of the test samples.

The base metal slabs of CM247LC and Rene 80 provided by Siemens were nominally 0.0256 m × 0.128 m × 0.218 m (1 in. × 5 in. × 8.5 in.). The samples were fabricated in blocks 0.128 m × 0.0513 m (5 in. × 2 in.) using the jig geometry shown in Figure 9. Three blocks were bonded for each base metal type along with one backing plate (grooved to allow the release of Zn vapor during the bonding process). The test samples machined from the joined parts were nominally 0.0254-m-diameter cylinders.

For the finite-element modeling, all materials in the assembly in Figure 9 were assumed to remain elastic except for the E52100 steel. A temperature-dependent, bilinear, isotropic hardening law was implemented for the plastic deformation of the steel based on Simsir and others [3]. The Young's modulus of the steel was also assumed to be temperature-dependent according to data from Shi and Liu [4]. All other material properties were assumed to be temperature-independent, with the exception of the linear coefficient of thermal expansion which was measured previously in this project and reported in Braband and in Tatsinkou-Nguelo [5, 6].

Figure 10 shows an image of the grooved backing plate that is used to hold the APMT to the base metal. The backing plate is fabricated from the same material as the base metal. The surface of the backing plate is grooved to allow zinc that has diffused through the APMT layer to reach vacuum and vaporize. To prevent the backing plate from bonding to the top of the APMT, the backing plate was heated to approximately 1000°C for 1 week in air prior to diffusion bonding. Previous tests have shown that the resulting oxidation layer is sufficient to prevent diffusion bonding at the APMT–backing plate interface.

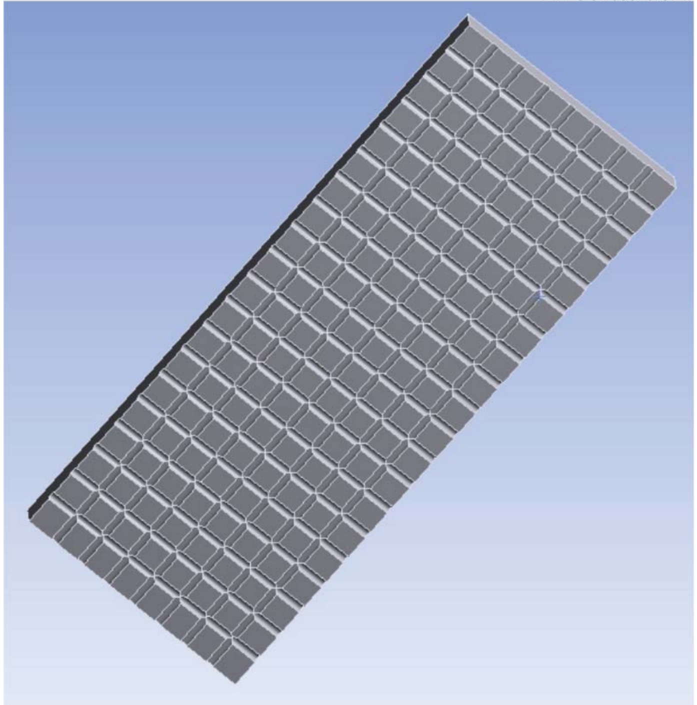
EERC JH50575.CDR

Figure 9. Grooved backing plate used to clamp the APMT to the base metal layer while allowing Zn to vaporize after reaching the top of the APMT layer.

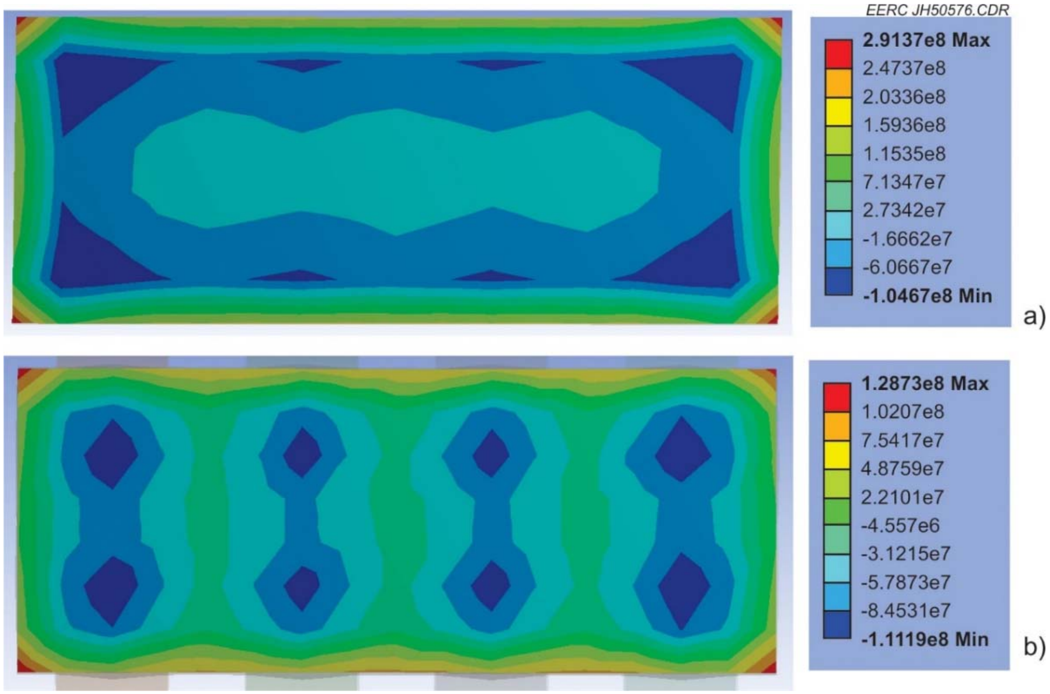

EERC JH50576.CDR

Figure 10. APMT–base metal interface normal stresses for a) CM247LC and b) Rene 80 at 1200°C.

Figure 11 shows the predicted normal stresses at the interface between the APMT and the base metal at 1200°C for both base metal types. Stresses are given in pascals, with negative values signifying compression and positive values signifying tension. With the exception of, at most, 6 mm at the outer edge, the entire surface is predicted to remain under compressive loading throughout the bonding process. Also, it is clear that the presence of the grooves on the face of the backing plate does not produce a nonuniform normal stress distribution on the bonding face. It should be noted that the compressive stresses on this face are expected to be artificially low, again because of the "bonded" condition between the backing plate and the APMT. Essentially, the APMT wants to expand more in the plane than the backing plate attached to it will allow, creating a tendency for the APMT to bow upward toward the backing plate, reducing the calculated compressive stress on this surface. The stresses within the plane of the APMT caused by this boundary condition are shown in Figure 11. In practice, this effect should be much lower, as the APMT will not be prevented from expanding except by friction. The calculated elevated equivalent stresses are arising because of the interface condition chosen for the finite-element modeling. To achieve convergence at all temperatures, all interfaces had to be set to "bonded." In practice, lateral motion of adjacent surfaces due to difference in thermal expansion, for example, is possible. In the model, it is not. This additional constraint produces artificially high equivalent stresses in the lower region of the joint that will not actually occur during fabrication.

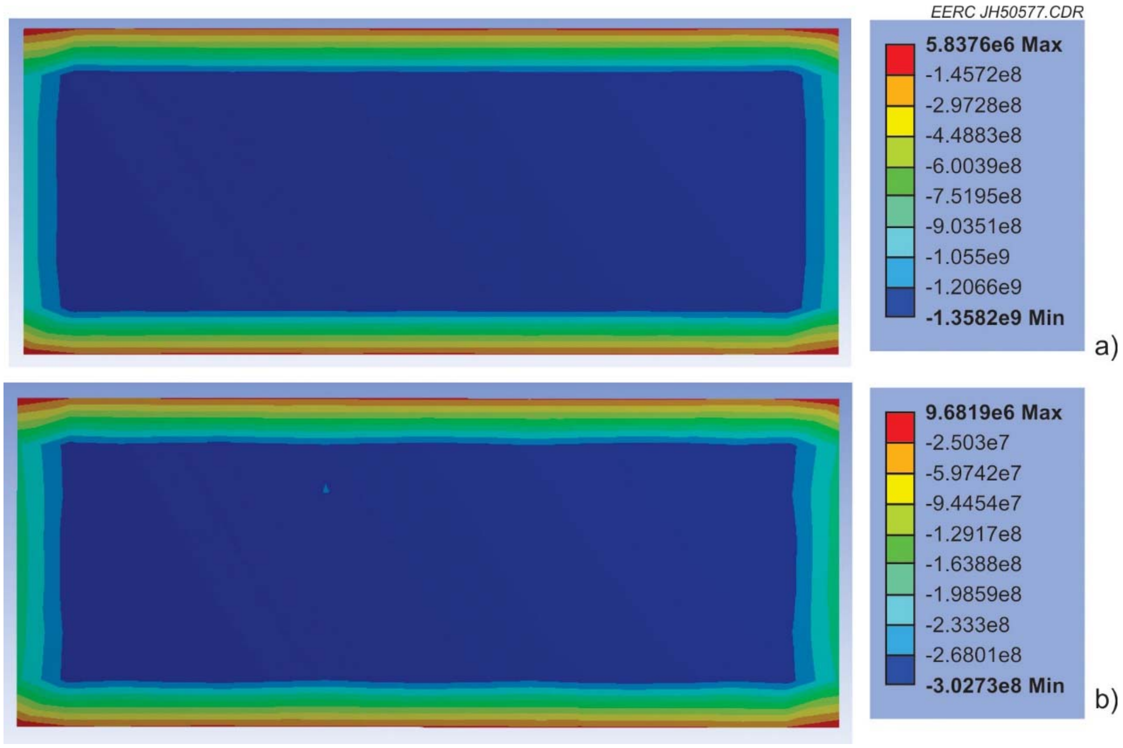

Figure 11. Normal stresses in the plane of the APMT for a) CM247LC and b) Rene 80 at 1200°C.

Based on the finite-element results, the jig assembly shown in Figure 8 should be able to successfully fabricate the samples for further oxidation/spallation/corrosion testing. Moreover, the general approach to designing jigs for larger/more complicated assemblies (i.e., a series of narrow jigs relatively closely spaced rather than a single continuous clamping plate) seems to be able to maintain the requisite bonding stresses while minimizing the jig material needed and the complexity of jig manufacturing.

Preparing the APMT-Plated Superalloy Blocks

After the modeling of the clamping system was completed, the jig parts were machined from blocks of TZM. Figure 12 shows the individual pieces. Figure 13 shows the pieces as assembled in preparation for heating to bond the APMT plate to the surface of the nickel superalloys.

After the first blocks of each superalloy were bonded, two 5-mm-thick sections were cut from one end of each of the bonded blocks using EDM and polished for analysis in a FEI Quanta™ FEG 650 series scanning electron microscope. The preliminary analyses were done to make sure that the bonds were complete, to determine whether or not the zinc had completely evaporated from the APMT and superalloys, and to determine what sort of interactions occurred between the APMT and superalloys.

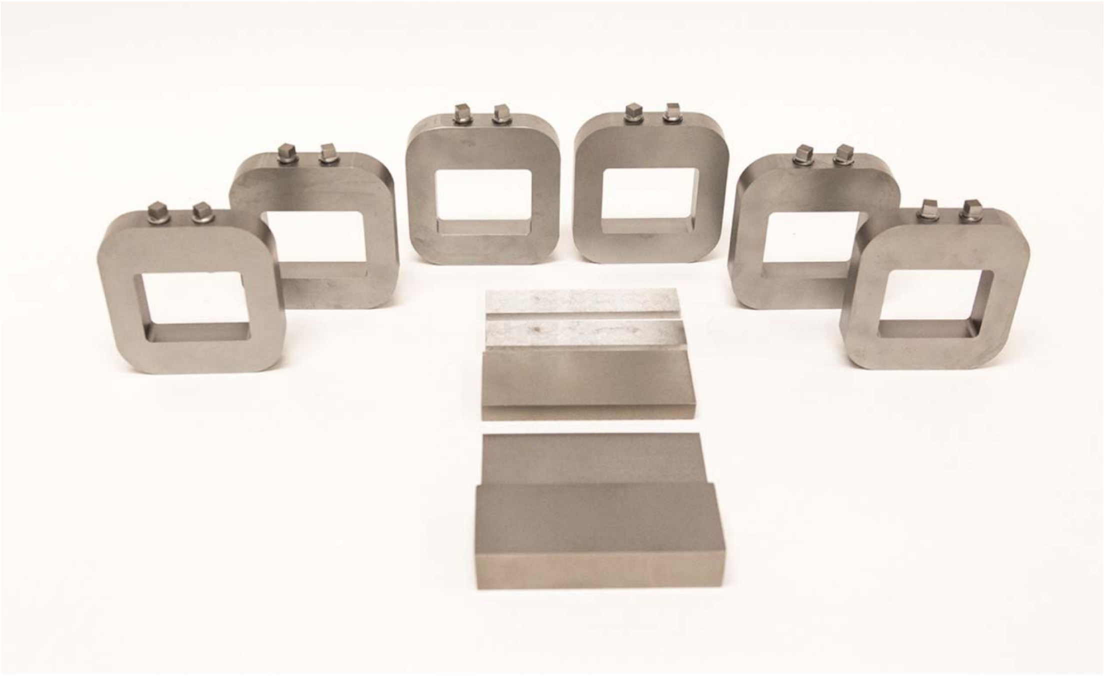

EERC JH51011.AI

Figure 12. Clamping jig and parts to be bonded.

Figure 13. Assembled jig in preparation for heating to bond the APMT plate to the superalloy block.

After determining that no zinc remained in the alloys being joined by SEM analyses, the remaining blocks were bonded. It was found that one bond for each superalloy was weak, possibly because the superalloy oxidized at room temperature enough to prevent the bonding since they were sandblasted approximately 1 month before bonding or because the sandblasting was inadequate in removing all of the surface scale. The other bonded pieces were sandblasted a second time the day before bonding and appear to have strong bonds.

One-inch-diameter cylindrical buttons underwent EDM from each of the bonded blocks. A total of 16 CM247LC buttons and 19 Rene 80 buttons were prepared and shipped to Siemens, which has performed precipitation hardening of the superalloys. Siemens will perform standard oxidation, spallation, and corrosion testing of the buttons. By performing the same tests that they have already done on the APMT and the two superalloys, we will be able to directly compare those results to the results for the APMT–superalloy bonded parts. However, as of the end date of this project (June 30, 2016), these tests had not yet been performed because other commercial work caused the testing to be postponed.

SEM Analyses of the APMT–Superalloy Bond Lines

SEM analyses were performed to determine the magnitude of the diffusion-affected zone in the non-precipitation-hardened samples. In addition, microindentation hardness testing was performed across the bond lines. These analyses were performed on the as-bonded specimens. Siemens has heat-treated the bonded samples in order to produce precipitation-hardened samples. It was originally intended to analyze the hardened samples as well, but the treatments were done just a few weeks before the end of the project, and the graduate student performing the analyses had recently graduated so the hardened samples were not analyzed. Siemens had been delayed in performing the heat treating because of demands on its furnace by commercial activities.

An FEI Quanta FEG 650 series scanning electron microscope with an accelerating voltage of 15 kV was used for imaging the as-bonded joints. Figures 14 and 15 show the bond lines between APMT and the superalloys. The figures show that large amounts of precipitates formed near the bond line, likely due to diffusion of nickel from the superalloys into the APMT and iron from the APMT into the superalloys. The light precipitates are enriched in heavy elements such as hafnium, tungsten, and cobalt. Some darker precipitates were also seen that are enriched in aluminum oxide, indicating that even though the pieces being bonded had been sandblasted twice, the alumina scale was still not completely removed. In order to determine the amount of interdiffusion of elements, EDS was used to perform area scans that are represented in Figure 16. The area scans started at the bond and proceeded up into the APMT approximately 900 µm as well as 900 µm below the bond into each of the two superalloys. This figure is only a representation of the scans from 250 µm into the APMT and superalloys. It should be noted that the regions are defined by the center line of that area scan, i.e., the region spanning from 100 to 150 µm, recorded as 125 µm.

Two methods were used in order to compare and identify the diffusion-affected zone. First, a high-contrast circular backscatter (CBS) image was taken of both samples in order to visually inspect the depth at which precipitates formed into the APMT and superalloys. CBS uses backscattered electrons and allows for a greater contrast between heavier and lighter elements, making it an ideal method for differentiating the various precipitates. Precipitates formed as far as 260 µm from the bond in the CM247LC and only 40 µm from the bond in the Rene 80. In both samples, precipitates formed in the APMT up to 40 µm from the bond.

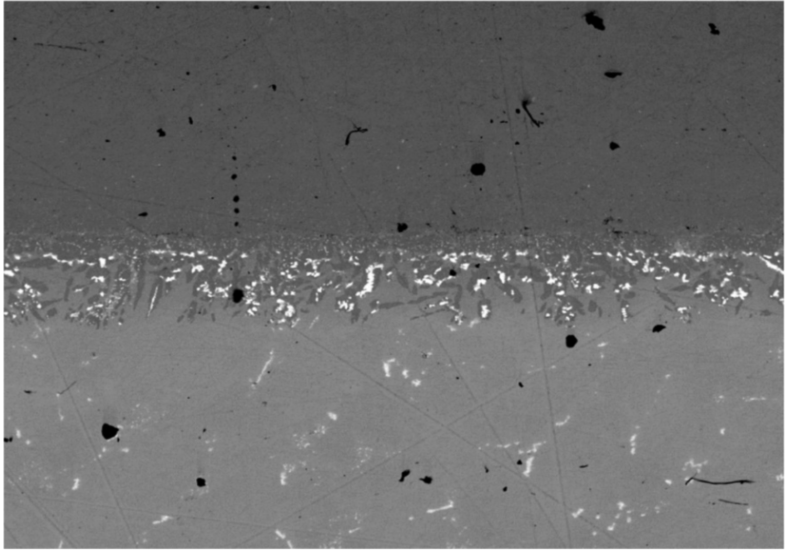

Figure 14. Bond line between CM247LC (bottom) and APMT (top) at 100× magnification.

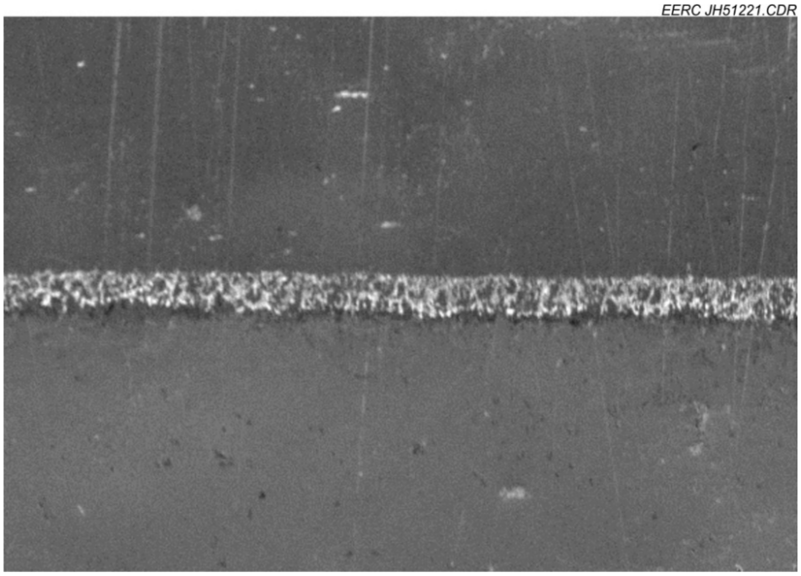
EERC JH51221.CDR

Figure 15. Bond line between Rene 80 (bottom) and APMT (top) at 100× magnification.

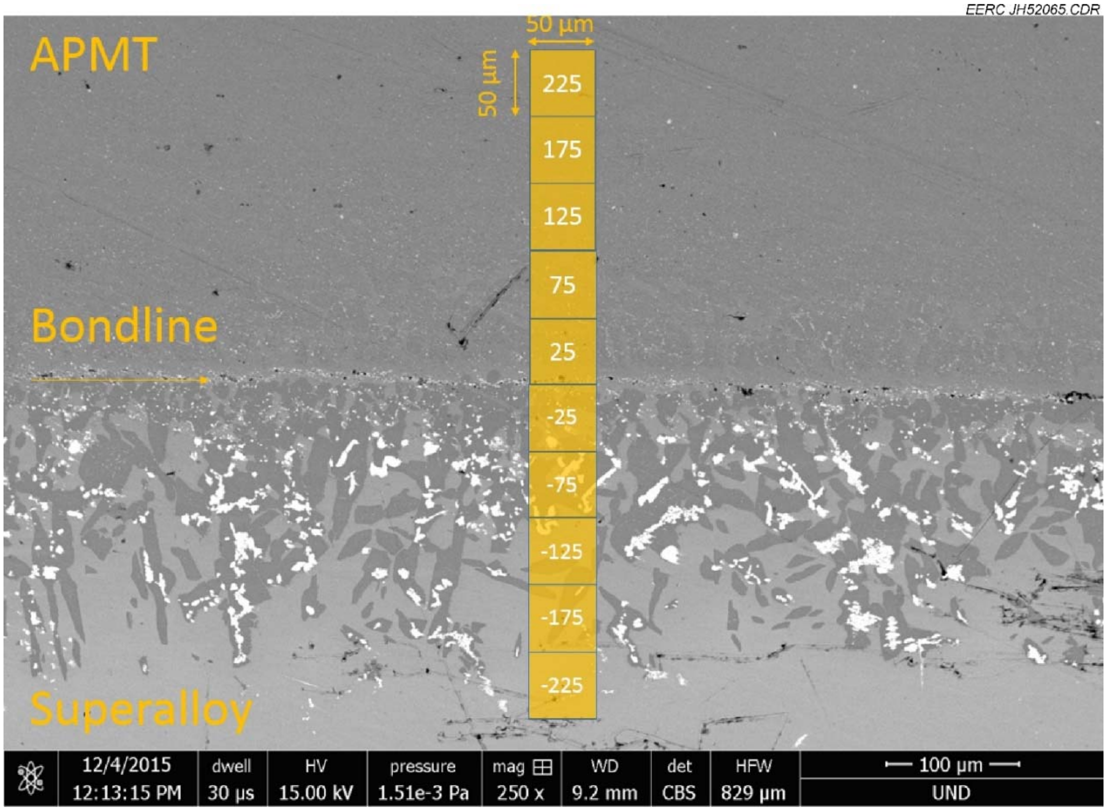
EERC JH52065.CDR

Figure 16. Representation of the SEM–EDS area scans.

EDS was then used to determine the compositions of 50-µm × 50-µm area scans, which were compared to the results of the CBS images. Each area scan is an average of two scans taken from different regions on each of the samples. The compositions were recorded as the scans progressed further into the APMT and the superalloys. Once the variation in composition became minimal (i.e., <0.5%), it was determined that the diffusion-affected zone had ended. The results of the data can be seen in Figures 17–26. For comparison purposes to the EDS data, the compositions of the base alloys are given in Table 1. The visual inspection determined where the heavier concentration of elements diffused, but the EDS results revealed that diffusion took place deeper into the structure as well as what elements were depleted from the materials' structure.

In both samples, nickel (Ni) diffused entirely through the APMT layer analyzed. In the Rene 80–APMT sample, it never exceeds 10 wt% composition and appears to be heavily depleted (>10%) within 50 µm of the bond in the Rene 80 and only moderately depleted (between 8% and 10%) throughout the 900-µm region examined. However, in the CM247LC–APMT sample, it is heavily concentrated, ranging from 11.3% to 35.3%, within the 350 µm into the APMT, but the CM247LC is only depleted within the first 250 µm from the bond and appears not to be depleted outside that.

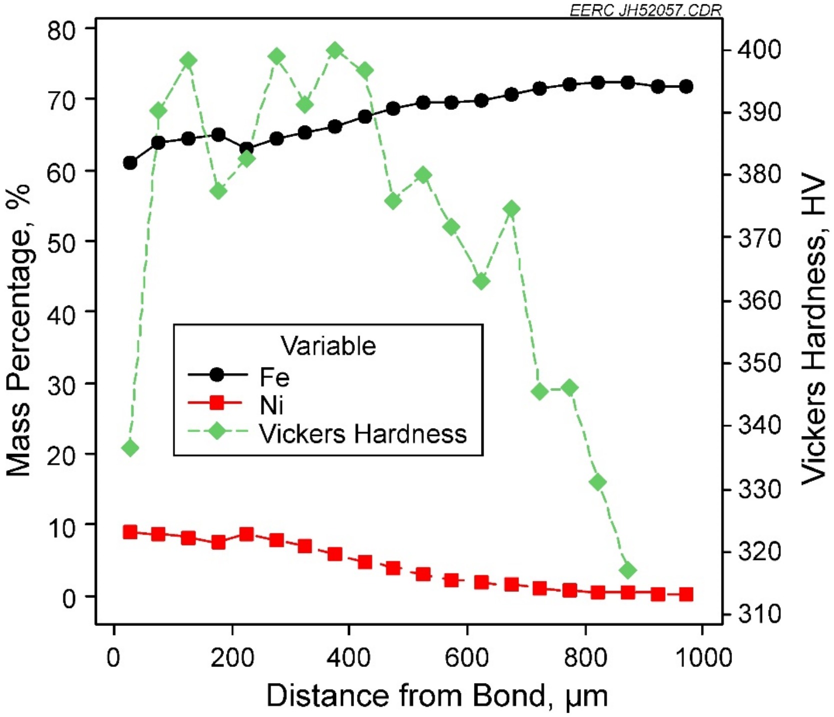

Figure 17. Concentration of Fe, Ni, and Vickers hardness vs. the distance from the bond into the APMT of the Rene 80–APMT sample.

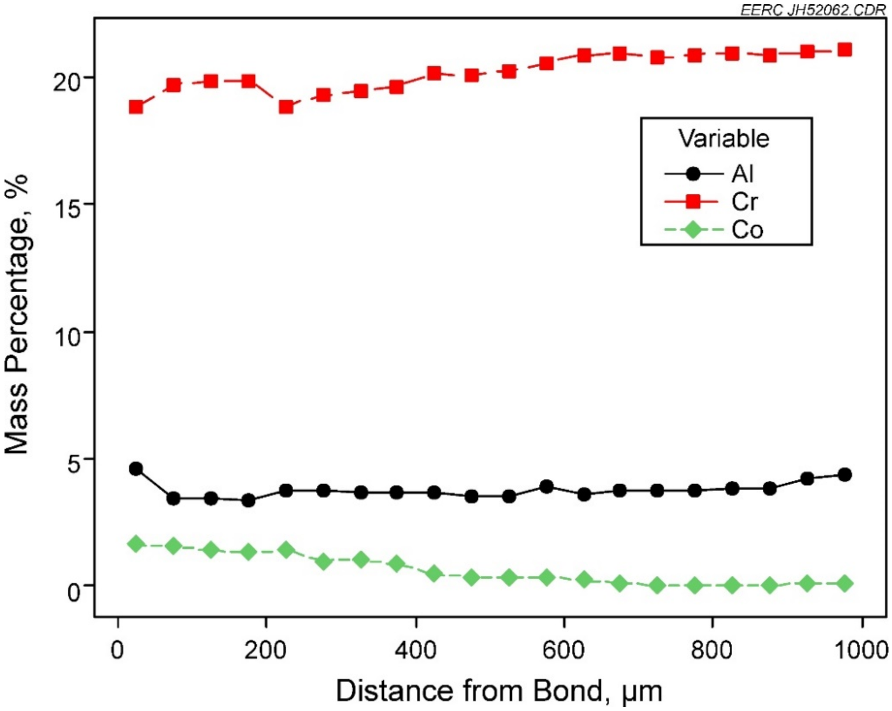

Figure 18. Concentration of Al, Cr, and Co vs. the distance from the bond into the APMT of the Rene 80–APMT sample.

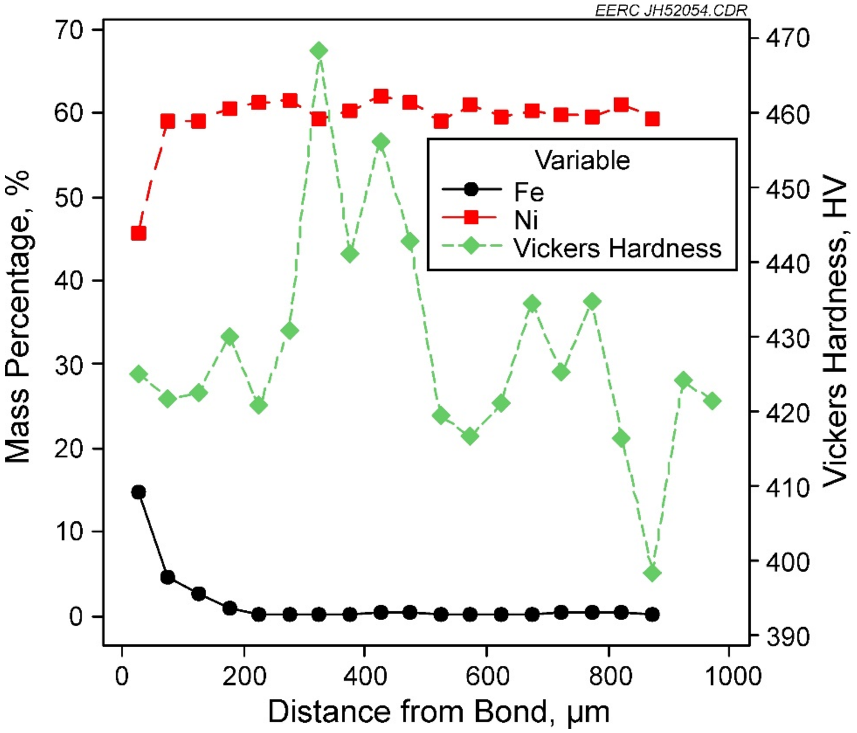

Figure 19. Concentration of Fe, Ni, and Vickers hardness vs. the distance from the bond into the Rene 80.

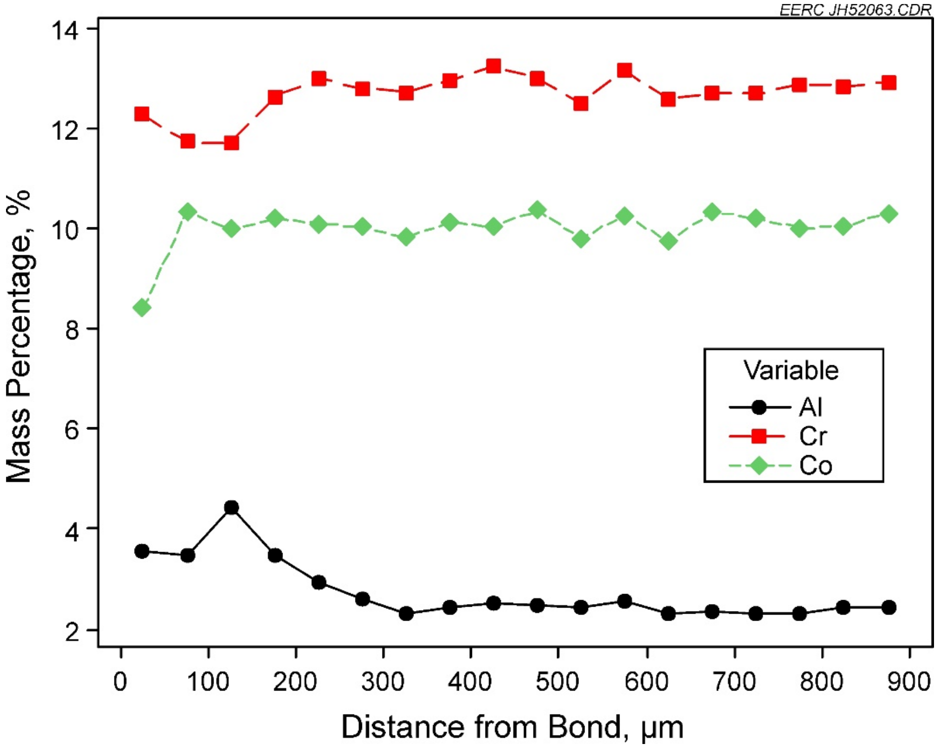

Figure 20. Concentration of Al, Cr, and Co vs. the distance from the bond into the Rene 80.

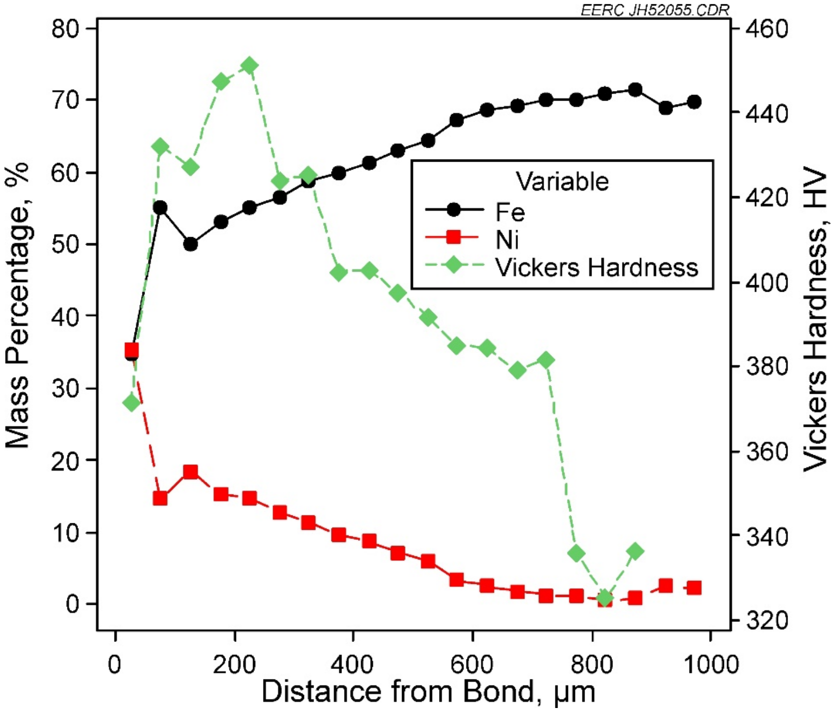

Figure 21. Concentration of Fe, Ni, and Vickers hardness vs. the distance from the bond into the APMT of the CM247LC–APMT sample.

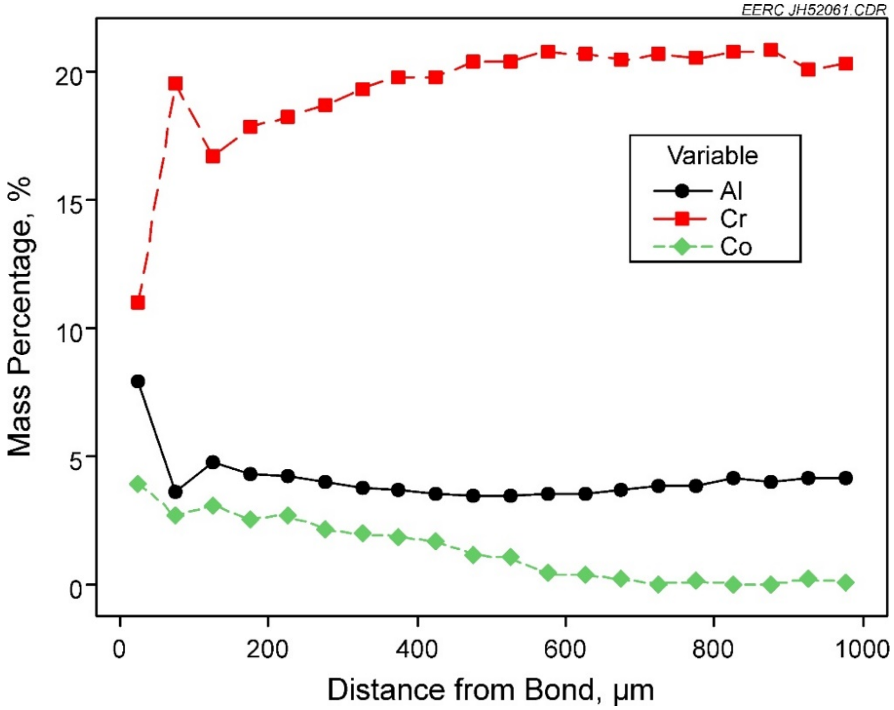

Figure 22. Concentration of Al, Cr, and Co vs. the distance from the bond into the APMT of the CM247LC–APMT sample.

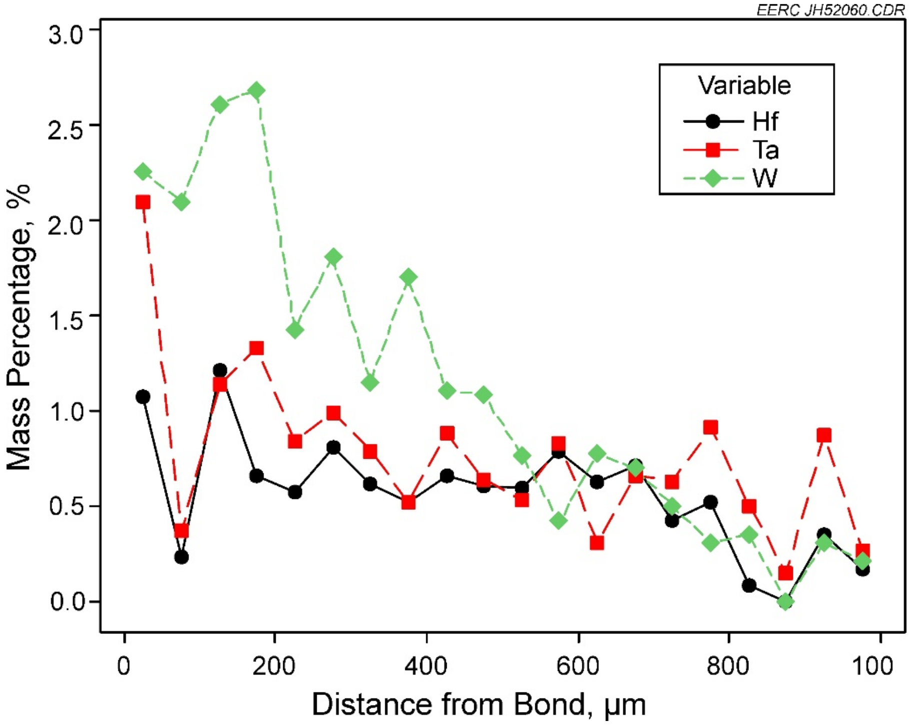

Figure 23. Concentration of Hf, Ta, and W vs. the distance from the bond into the APMT of the CM247LC–APMT sample.

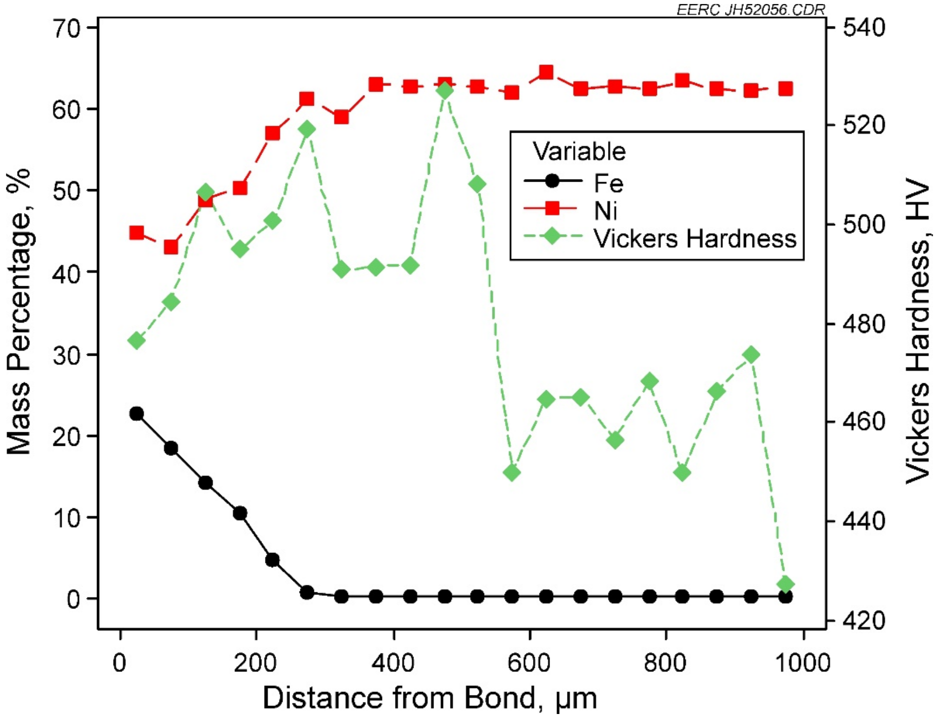

Figure 24. Concentration of Fe, Ni, and Vickers hardness vs. the distance from the bond into the CM247LC.

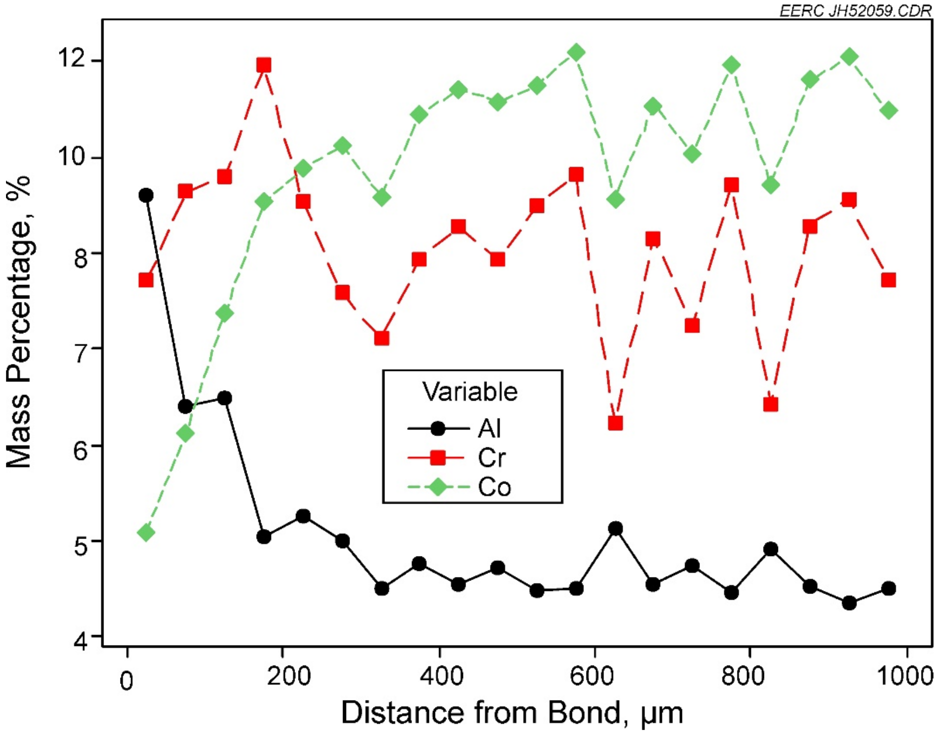

Figure 25. Concentration of Al, Cr, and Co vs. the distance from the bond into the CM247LC.

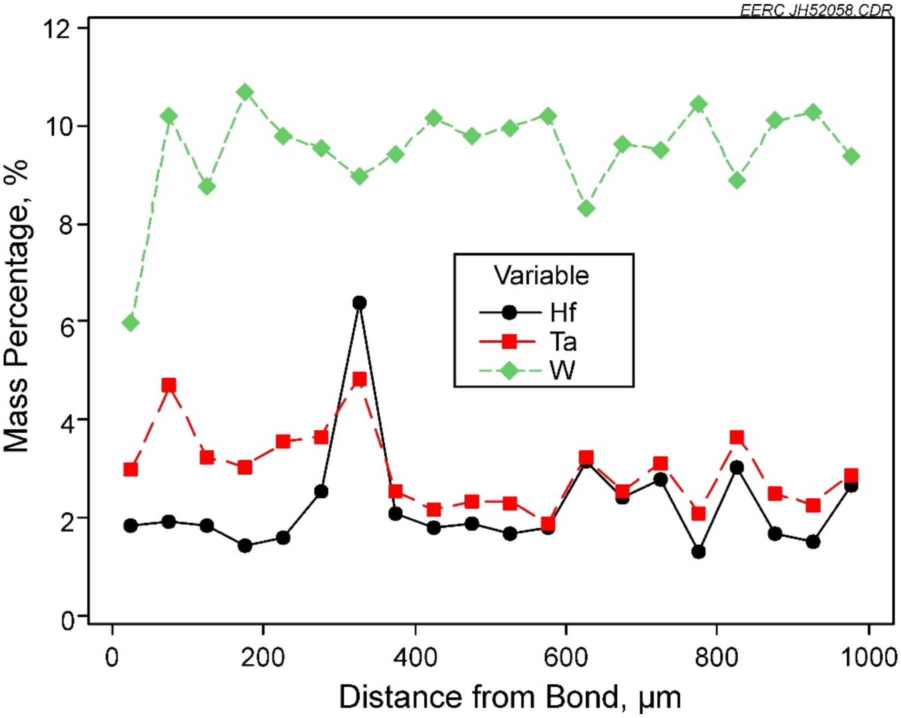

Figure 26. Concentration of Hf, Ta, and W vs. the distance from the bond into the CM247LC.

Iron (Fe) also appears to have diffused from the APMT into both superalloys spanning the entire 900 µm examined; however, it is very concentrated up to 150 µm in the Rene 80 and 250 µm in the CM247LC. Fe appears to be moderately depleted from the APMT in the Rene 80 sample up to 400 µm but more heavily depleted in the CM247LC sample.

Chromium (Cr), aluminum (Al), and cobalt (Co) are much less diffused and are within 0%–3% of their initial compositions of the base alloys throughout the entire region analyzed. Hafnium (Hf), tantalum (Ta), and tungsten (W) also diffused at low rates. However, around the 250–350-µm region, we see a significant increase of Hf and Ta. Large, white, and amorphous precipitates formed during the EMB process in this region. They were extremely high in Ta (57.0%) but relatively low in Hf (3.5%).

A Mitutoyo HM-112 Micro Vicker hardness-testing machine was used to determine the hardness of each sample as a function of distance from the bond lines. The Vickers number was used to correlate the materials' hardness to the diffusion and formation of certain elements and precipitates. Testing was done similarly to that of the EDS area scans, where an initial measurement was taken approximately 25 µm from the bond (the center of the scanned region) and every subsequent measurement after that was 50 µm from the last as it proceeded further into each material; a load of 0.2 kg was applied over 12 seconds. A total of three tests were performed at each depth throughout the sample in order to attain an average hardness for every 50-µm increment. The results for the hardness testing were overlaid onto the same graphs as the most heavily diffused elements (iron and nickel). These results can be seen in Figures 17 and 19 for the Rene 80–APMT sample and Figures 21 and 24 for the CM247LC–APMT sample. The figures show that the material is weakest deeper within the APMT and superalloys than at the bond lines, possibly indicating that the precipitates that formed during the bonding process had hardened the materials. This is in line with the results of the initial high-temperature tensile strength testing done previous to the UTSR Program, where the bonded alloys always broke within the APMT rather than at the bond or in the superalloys. It should be noted that the superalloys boast a much higher hardness value than that of the APMT, which is the reason why in tests previous to the UTSR Program the materials fracture within the APMT rather than the superalloys.

Gasifier Sampling

Gas sampling was performed from the EERC FBG and EFG systems to determine the types and concentrations of microcontaminants in the gas that could reach a turbine firing coal-derived syngas. Gas sampling was performed during at least five gasifier runs. However, early sampling runs were often contaminated with rust originating in the TOX. The results presented here show particles that were collected after sampling procedures had been modified to prevent the collection of rust. Data from the analyses of the impinger solutions are not given because the concentrations of elements detected in the solutions were near or below the minimum detectable concentration ranges.

Samples Collected During Testing with the Pressurized FBG

Particulates were collected at both the inlet and the outlet of the TOX while the pressurized FBG was firing a subbituminous coal from the Eagle Butte Mine, Wyoming. No sulfur removal technology was used during the gasifier test. Four samples were collected, two immediately before the TOX and two at the bottom of the TOX. The first and second tests were conducted at the inlet before the combustor, while the third and fourth tests were conducted at the outlet after combustion.

We attempted to analyze these filter samples in the EERC JEOL 5800 SEM equipped with an Oxford Instruments INCA EDS system and a silicon drift x-ray detector. However, measurable x-ray signals could not be obtained with the EERC EDS system because the particles were so small, so the compositions of the particles could not be determined. Therefore, a piece of the filter sample collected from the inlet to the TOX was sent to JEOL USA for analysis by Natasha Erdman with a more powerful field emission-type SEM.

Figure 27 shows an image of the inlet particles with the JEOL USA system. The particles captured at the inlet have diameters typically between 0.2 and 0.5 µm. Figure 28 is composed of two higher-magnification images of the same area. Figure 28a is taken using secondary electron imaging (SEI), whereas 28b is taken using backscatter electron imaging (BEI). In BEI imaging, the contrast is modified by the density of the particles, denser particles appearing brighter than less dense particles. The images show that a few of the particles are denser than the majority of the particles and, therefore, likely contain higher-atomic-number elements such as sulfur. It also shows that many of the larger particles are composed of conglomerates of 0.1-µm particles. However, JEOL USA was also not able to obtain sufficient EDS data from the small particles for identification, other than carbon and sulfur, which could have been interference from x-rays emanating from the underlying filter. The small black circles are holes in the filter.

EERC JH48365.CDR

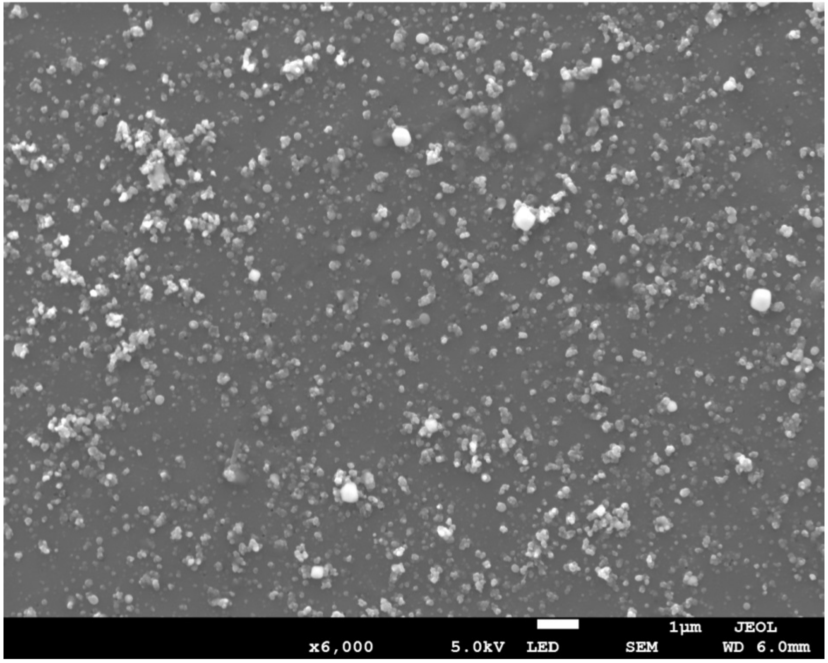

Figure 27. SEI image of particles collected on the filter at the TOX inlet.

EERC JH48368.CDR

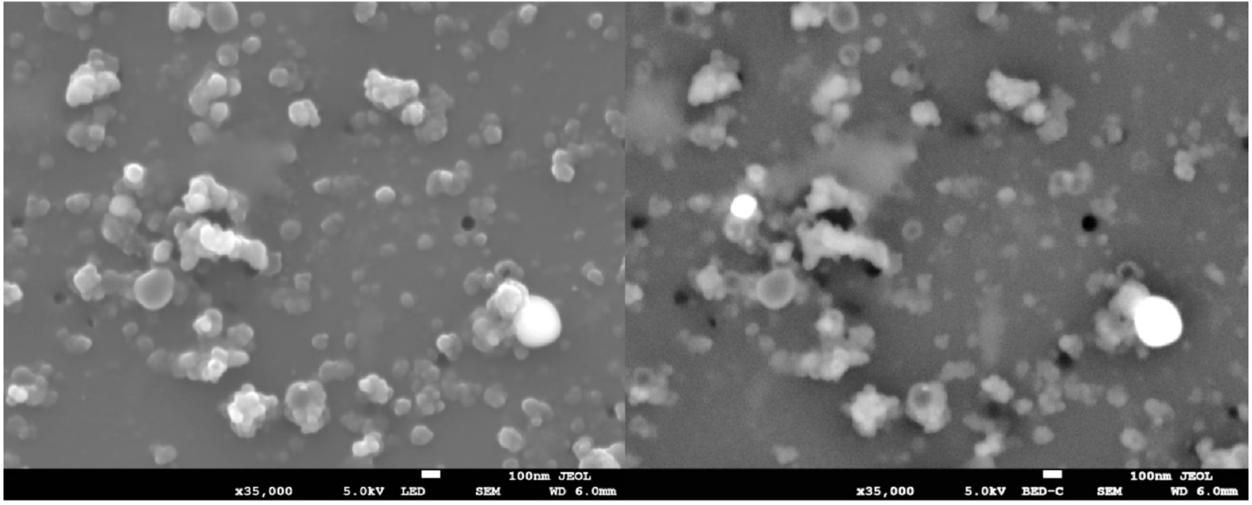

2a 2b

Figure 28. Higher-magnification views of the same area showing the differences between SEI (2a) and BEI (2b) images.

Figure 29 is an SEI image taken with the EERC SEM showing particles collected on the filter at the outlet of the TOX. The image shows that the particles are somewhat larger and more spherical than those at the inlet to the oxidizer. As with the inlet particles, the EDS data were not conclusive as to the compositions of these particles, although more oxygen was detected.

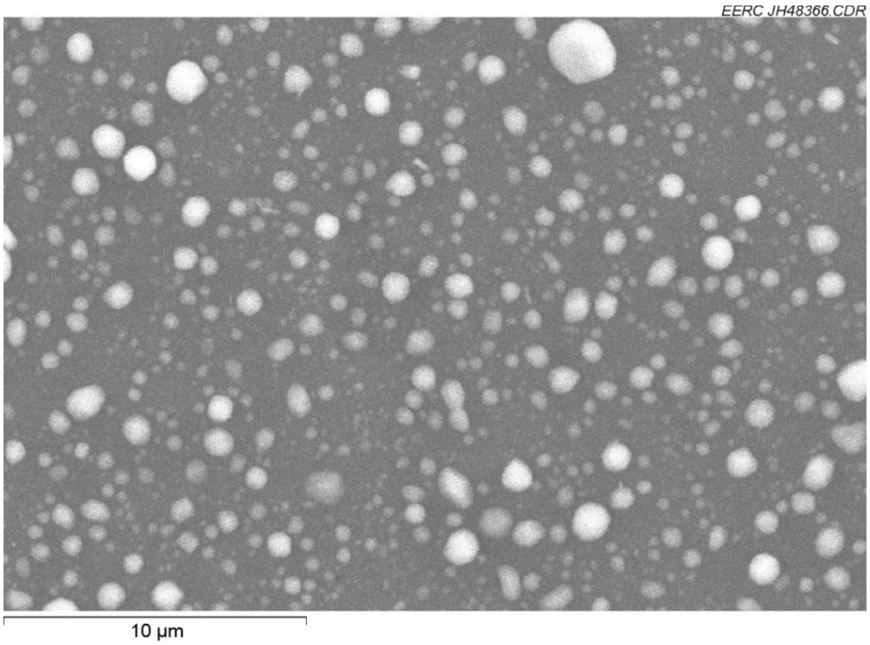

Figure 29. SEI image of particles collected on the filter at the TOX outlet.

Figure 30 is an SEI image taken with the EERC SEM showing particles collected on the filter at the outlet of the TOX when no syngas was being burned in the oxidizer. It shows that the particles collected are much smaller and much less concentrated than the filter samples collected from the syngas and from the syngas combustor.

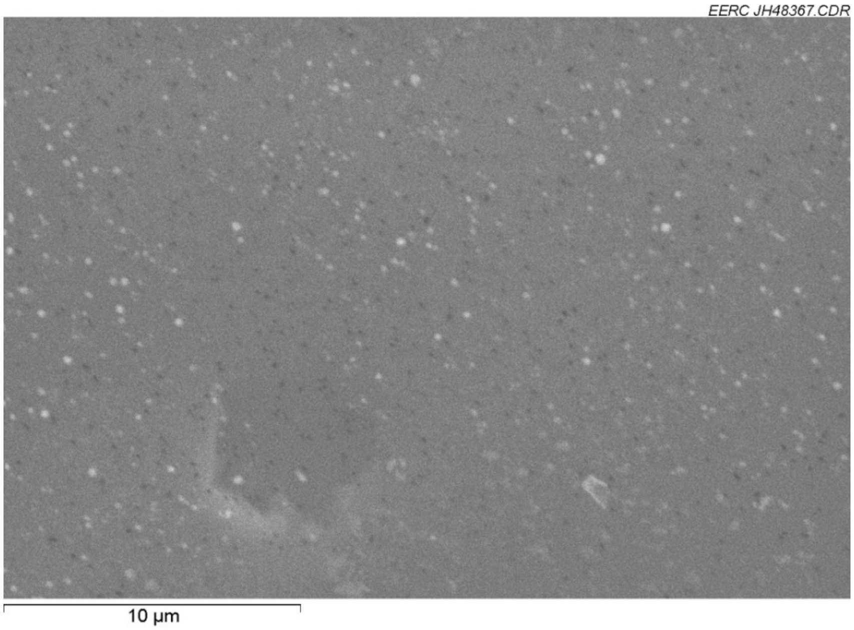

Figure 30. SEI image of particles collected on the filter at the TOX inlet when no syngas was being burned.

Because the EDS signals collected for the particles both at the EERC and JEOL USA were not conclusive as to the compositions of the particles collected on the filters, the EERC applied for time on electron microscopes using different signal analyzers at the Oak Ridge National Laboratory (ORNL) ShaRE User Facility, which is sponsored by the U.S. Department of Energy Scientific User Facilities Division of the Office of Basic Energy Sciences. The analyses were performed by Karren More and Henry Meyer III. At ORNL, both x-ray photoelectron spectroscopy (XPS) and Auger electron spectroscopy (AES) were performed on the samples because these are surface analyses that analyze electrons emitted from within a few nanometers of the surfaces of the particles and filters. In XPS, areas of the filter on which particles reside are analyzed. In AES, individual particles can be analyzed, but this type of analysis was not found to be useful because it was hampered by excessive charging of the samples because of their nonconductive nature.

Figures 31–33 show summaries of the findings of the XPS analyses. In Figure 31, the electron spectrum for the TOX inlet sample containing both particles collected from the unburned syngas and filter area is compared to the spectrum for just the filter. The data show that the particles do not contain any metals and, in fact, have an atomic composition almost identical to that of the polycarbonate filter. We currently believe that this indicates that the particles are primarily soot-based and not formed from volatilization of metals in the gasifiers. Figure 32 compares the spectra for particles collected from the syngas to the particles collected from the combusted syngas. Filter area is also included in the analyses. The data indicate that the soot-based particles are not well burned in the TOX, although they are significantly oxidized, nitrided, and sulfidized in the combustor.

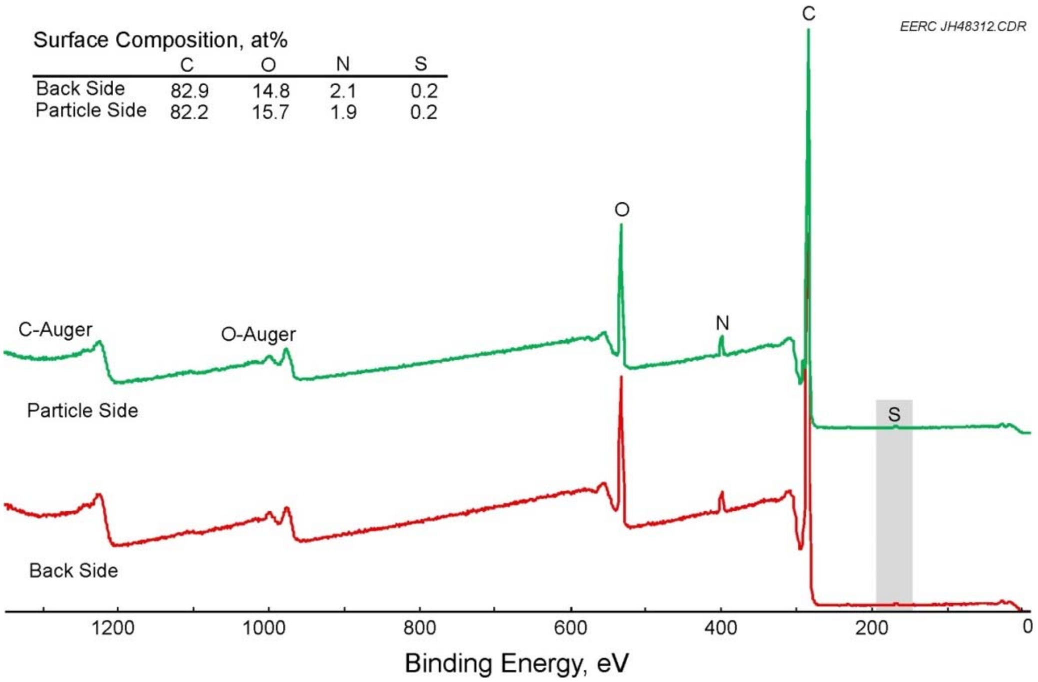

Surface Composition, at%

	C	O	N	S
Back Side	82.9	14.8	2.1	0.2
Particle Side	82.2	15.7	1.9	0.2

Figure 31. XPS spectrum for an area on the front side (filter + particles) of the filter sample collected from the inlet to the TOX on March 13, 2013, compared to the spectrum collected from an area on the back side (just filter material).

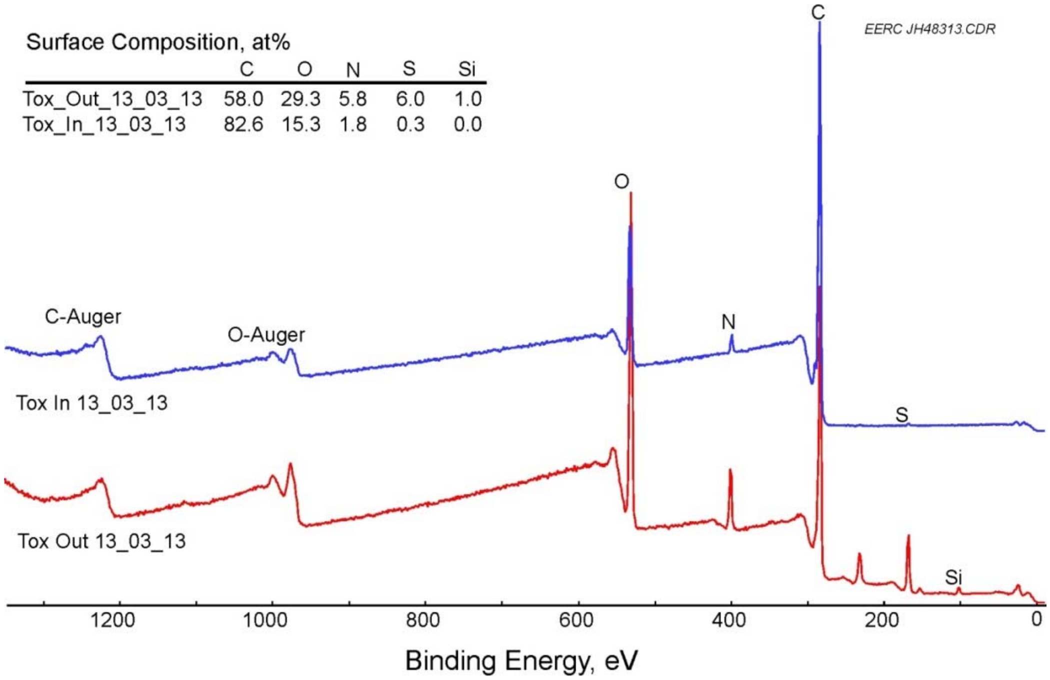

Figure 32. XPS spectra for an area of the filter covered with particles collected from the inlet of the TOX (blue) compared to an area of the filter covered with particles collected from the outlet of the TOX (red).

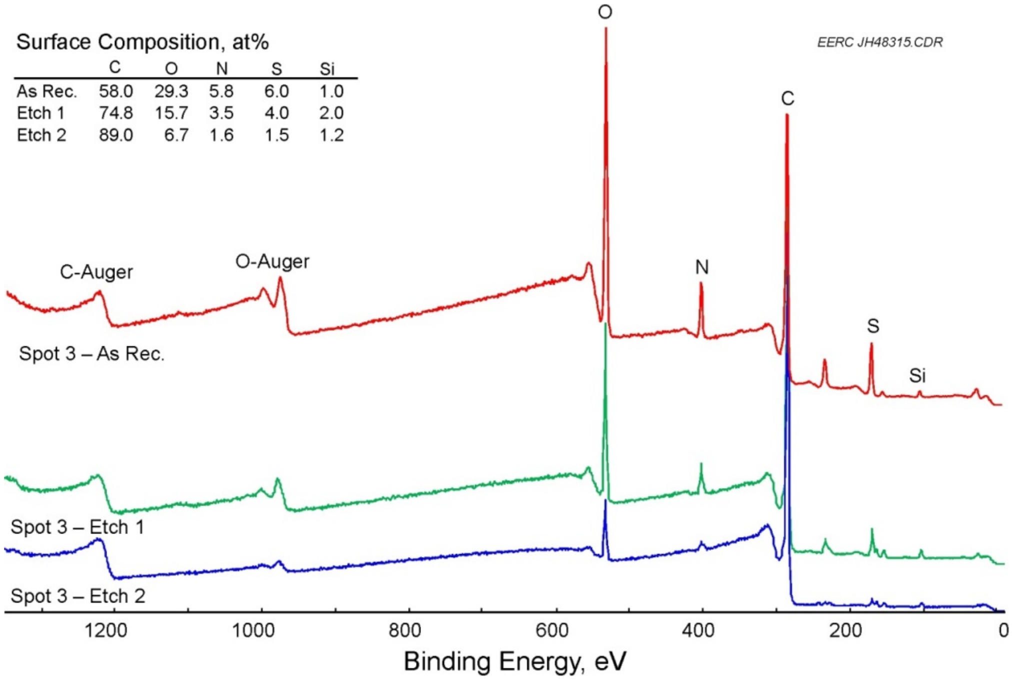

Figure 33. XPS spectra for an area of the filter covered with particles collected from the outlet of the TOX before ion etching (red) and after one (green) and two (blue) etching cycles.

Figure 33 shows data for the TOX outlet particles as well as spectra for the same areas after one and two ion etchings. The etching removes the outer layers of the particles. The data indicate that the oxidation, nitridation, and sulfidation of the particles are primarily surface phenomena.

Samples Collected During Testing with the Pressurized EFG

Sampling was performed at both the inlet and the outlet of the TOX while the EFG was firing subbituminous coal from the Antelope Mine in Wyoming. Three samples were collected: one at the inlet of the TOX and two at the outlet. The first sample was collected at the outlet while coal syngas was being fired, the second was collected from the coal syngas at the inlet to the TOX; and the third sample was collected at the TOX outlet while firing on natural gas only. During these sampling periods, a total syngas volume of 153.25 ft^3 was collected in the sampling train, with 56.8 ft^3 (1.61 m^3) for the first sample, 49.0 ft^3 (1.39 m^3) for the second, and 47.5 ft^3 (1.34 m^3) for the third. Particulate loadings were 0.808 mg/m^3 at the TOX outlet when syngas was fired, 6.906 mg/m^3 at the TOX inlet, and 0.698 mg/m^3 at the TOX outlet when only natural gas was fired.

Initial analyses of the particles were performed with the EERC JEOL 5800 SEM. However, that SEM has relatively low resolution, so it was decided to repeat the analyses using a high-resolution SEM on the UND campus. The new UND field emission SEM is an FEI Quanta 650 FEG. The samples analyzed were cut from the filter and mounted on a carbon plug using carbon paint to hold them to the plugs. The samples were lightly coated with evaporated carbon to increase the electrical conductivity of their surfaces. Figure 34 shows the particles collected at the outlet of the TOX while syngas and natural gas were being fired in the TOX. The particles are primarily 0.05 to 0.2 µm in diameter. EDS of individual particles indicates that they all consist of approximately 89% carbon, 9% oxygen, and 1% nitrogen. Although we can expect that the EDS results would be heavily contaminated by x-rays from the filter (polycarbonate), we should have seen some signals from any metals that were present, indicating that they are essentially all soot particles and not formed from vaporized metals that condensed in the cooler syngas stream. This is consistent with the results from sampling while operating the FBG system which were also essentially soot. This indicates that little to no vaporized metals made it past the warm-gas filters and scrubbers in the gasifier system.

Figure 35 shows particles collected at the inlet to the TOX which were present in the unburned syngas. Even though this filter showed the highest weight gain during sampling, essentially no soot particles were found on the surface of the filter. However, there were large flakes of iron oxide containing some sodium, chlorine, sulfur, and zinc. Figure 36 shows one of these flakes. It is 200 µm long and 100 µm across. The flakes are what make up the weight gain measured for the filter. The lack of submicrometer soot particles is likely due to the very high operating temperature (1800°C) of the EFG, which reduces both soot and tar formation. However, soot particles form during combustion of the syngas in the TOX, as shown in the last quarterly report.

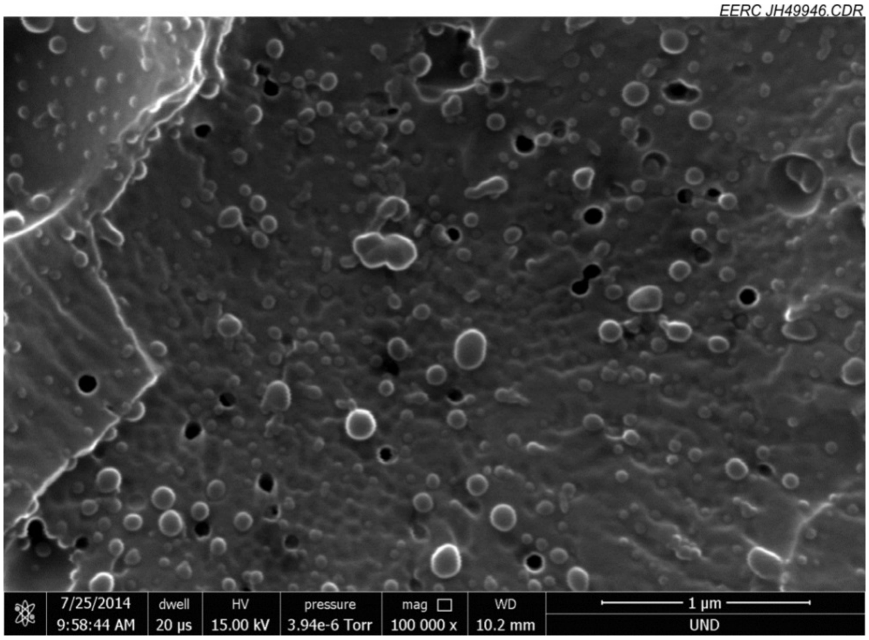

Figure 34. Particles collected at the outlet of the TOX while syngas and natural gas were being fired in the TOX.

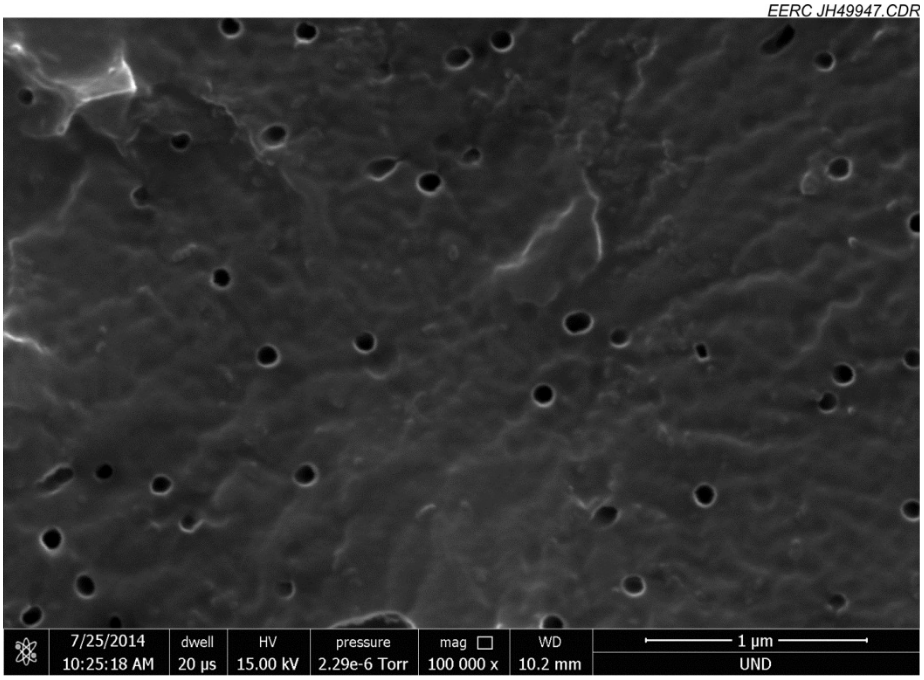

Figure 35. Particles collected at the inlet to the TOX which were present in the unburned syngas.

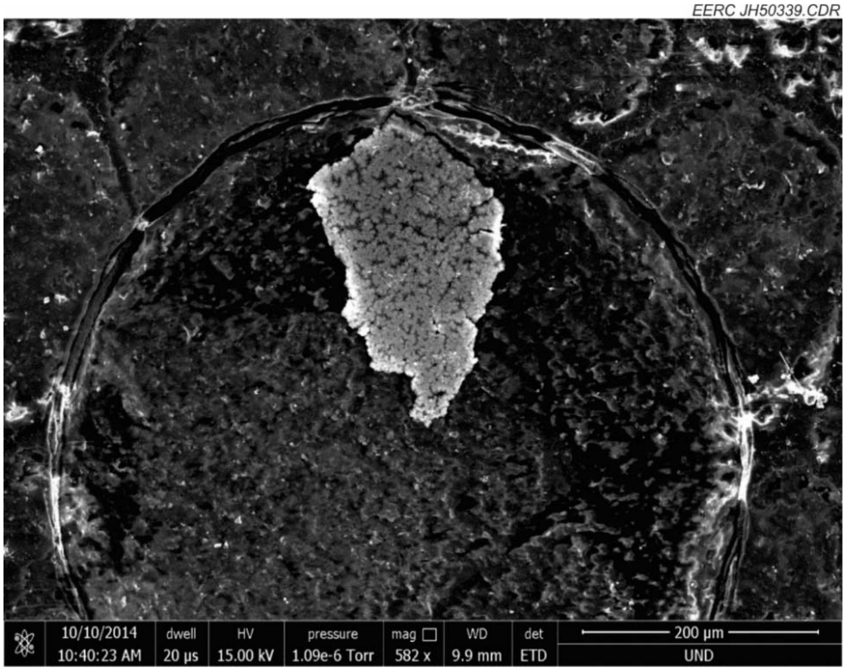

Figure 36. Large flake of iron oxide collected at the inlet of the TOX.

Figure 37 shows particles collected at the outlet of the TOX while it was burning only natural gas. These particles are smaller than those collected from the syngas at the TOX outlet but, like those particles, consist only of carbon, oxygen, and a small amount of nitrogen.

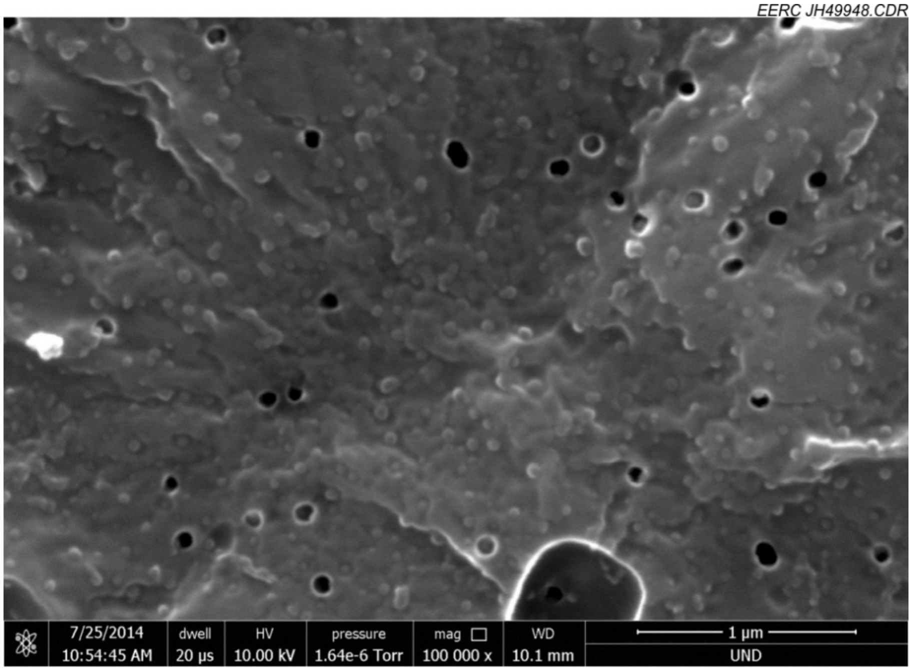

Figure 37. Particles collected at the outlet of the TOX while it was burning only natural gas.

These results indicate that the particles that were collected consist almost entirely of submicrometer soot and that little to no vaporized metals made it past the warm-gas filters and scrubbers in the high-temperature EFG system which could then deposit in a turbine system burning a higher-hydrogen syngas. In addition, there were large flakes of iron oxide that likely formed on gasifier steel surfaces that could reach the turbine combustor. These results are consistent with the analyses of the particulates collected when the lower-temperature FBG system is used. Because only soot was the main type of particulate matter collected, it was decided that corrosion testing of the APMT-plated superalloys under Task 6 should be done by Siemens using its standard corrosion test method so that the results could be compared more directly with previous corrosion tests of the unplated alloys. Unfortunately, as of the time of this report (August 30, 2016, 2 months after the end of the project), Siemens was not able to complete either the corrosion or oxidation tests because of other commercial activities that precluded performing the tests in time. They agreed to perform these tests without funding from this UTSR project, and that work was not included in the cost share for this project. They had, however, started the spallation testing of the APMT-plated CM247LC at the highest temperature that they run those tests (1150°C). In those tests, several of the APMT plates separated from the CM247LC, likely because of the aluminum oxide that was present on the surface of the CM247LC. This implies that surface preparation may need to include machining to remove the oxide scale before bonding rather than just sandblasting. In previous (pre-UTSR Program) tensile strength testing of APMT–CM247LC joints that were surface-machined before bonding and tested at 950°C, the breaks in the tensile samples always occurred in the APMT and not at the joints.

CONCLUSIONS

We have found that we were unable to create joints when temperatures much lower than the original (pre-UTSR Program) temperature of 1214°C were used. Therefore, we limited our diffusion rate measurements to the two hold temperatures used in the procedure: 700° and 1214°C. The diffusivity of zinc in both APMT and CM247LC is quite similar at 700°C. At 1214°C, the situation is very different. The calculated diffusivity of zinc in APMT is approximately 15 times higher than in CM247LC or Rene 80 (~120 vs. ~8 μm^2/min) at that temperature.

In addition to the diffusion work, the coefficients of thermal expansion were determined for each of the alloys as a function of temperature. This information has been entered into a finite-element model using ANSYS so that appropriate force-applying structures can be designed for use in joining structures composed of APMT and the nickel alloys. The finite-element model was completed and used to design clamping jigs to hold 1-mm-thick APMT plate to the larger blocks of superalloys during the bonding process. The clamping system was machined from TZM because of its strength at temperature and lower coefficient of thermal expansion than any of the alloys being bonded. The bond between the APMT plate and the superalloys was weak enough that the plate fell off after processing for each of the superalloy blocks that were first bonded. We believe that this occurred because the alumina scale present on the surfaces of the blocks was not sufficiently removed before bonding. The other blocks were, therefore, more strongly sandblasted before bonding to the APMT. These joints were much stronger than the first joints prepared. SEM analyses of representative joints showed that no zinc remained in the alloys after bonding. Also, phases rich in hafnium and tantalum had precipitated near the bond line in the APMT. Iron from the APMT had diffused into the superalloys during bonding, more extensively in the CM247LC than in the Rene 80. Nickel from the superalloys had diffused into the APMT, again more extensively in the joint with the CM247LC than with the Rene 80. Unfortunately, the analyses also showed some small pieces of broken aluminum oxide scale near the bond lines. One-inch-diameter buttons were machined from each of the bonded blocks and sent to Siemens for standard oxidation, spallation, and corrosion testing, which was scheduled for completion in the spring of 2016. However, because of commercial demands on those at Siemens who were to do the testing, the tests were not completed by the time of this report except some initial spallation tests at 1150°C. In those tests, several of the APMT plates separated from the CM247LC, likely because of the aluminum oxide that was present on the surface of the CM247LC. This implies that surface preparation may need to include machining to remove the oxide scale before bonding rather than just sandblasting. In previous tensile strength testing of APMT–CM247LC joints that were surface-machined before bonding and tested at 950°C, the breaks in the tensile samples always occurred in the APMT and not at the joints.

Gasifier sampling was completed to determine what types of trace contaminants may occur in cleaned and combusted syngas and that could lead to corrosion or deposition in turbines firing coal syngas. The sampling was done from two EERC pilot-scale gasifiers that were being operated under funding outside of the UTSR program. One is a pressurized FBG, and the other a pressurized EFG. SEM analyses showed that the particles captured on the filter from the syngas were typically 0.2 to 0.5 µm in diameter, whereas those captured from the combusted syngas were slightly larger and more spherical. XPS was performed on the samples at ORNL. The data showed that the particles do not contain any metals and, in fact, have an atomic composition almost identical to that of the polycarbonate filter. We currently believe that this indicates that the particles are primarily soot-based and not formed from volatilization of metals in the gasifiers. The data indicate that the soot-based particles are not well burned in the TOX, although they are significantly oxidized, nitrided, and sulfidized in the combustor at the particle surfaces.

REFERENCES

1. Poirier, D.R.; Geiger, G.H. *Transport Phenomena in Materials Processing*; TMS: Warrendale, PA, 1994.

2. Butrymowicz, D.B.; Manning, J.R.; Read, M.E. Diffusion in Copper and Copper Alloys Part IV. Diffusion in Systems Involving Elements of Group VIII. *J. Phys. Chem. Ref. Data* **1976**, *5* (1), 103–200.

3. Simsir, C.; Dalgic, M.; Liibben, T.; Irretier, A.; Wolff, M.; Zoch, H.W. The Bauschinger Effect in the Supercooled Austenite of SAE 52100 Steel. *Acta Materialia,* **2010***, 58*, 4478–4491.

4. Shi, J.; Liu, C.R. On Predicting Chip Morphology and Phase Transformation in Hard Machining. *Int. J. Adv. Man. Tech*. **2006**, *27*, 645–654.

5. Braband, J. Characterization of Evaporative Metal Bonding in Superalloys for Use in Gasified Coal Turbine Generators. M.S. Thesis, University of North Dakota, Grand Forks, ND, 2013.

6. Tatsinkou-Nguelo, S. Preparation and Analysis of Evaporatively Bonded Superalloys for Use in Hydrogen Burning Gas Turbines. M.S. Thesis, 2014.